Endogenously generated Dutch-type Aβ nonfibrillar aggregates dysregulate presynaptic neurotransmission in the absence of detectable inflammation

Emilie L. Castranio[1], Merina Varghese[2-4], Elentina K. Argyrousi[5], Kuldeep Tripathi[6], Yong Huang[1], Akiko Asada[7], Linda Söderberg[8], Erin Bresnahan[3,4,9], David Lerner[3,4], Francesca Garretti[3,4], Hong Zhang[5], Jonathan van de Loo[5], Cheryl D. Stimpson[10,11], Ronan Talty[2,3,12], Charles Glabe[13], Efrat Levy[14], Minghui Wang[15], Marjan Ilkov[16], Toshiharu Suzuki[7], Kanae Ando[7], Bin Zhang[15], Lars Lannfelt[7], Brigitte Guérin[16], William D. Lubell[17], Shai Rahimipour[6], Dara L. Dickstein[3,4,9,10], Sam Gandy[1,18,19]†, Ottavio Arancio[5]†, & Michelle E. Ehrlich[1,14,20,*]†

[1]Department of Neurology, Icahn School of Medicine at Mount Sinai, New York, NY, 10029, USA.

[2]George & Anne Ryan Institute for Neuroscience, University of Rhode Island, RI, 02881, USA.

[3]Nash Family Department of Neuroscience, Icahn School of Medicine at Mount Sinai, New York, NY, 10029, USA.

[4]Friedman Brain Institute, Icahn School of Medicine at Mount Sinai, New York, NY, 10029, USA.

[5]Department of Pathology and Cell Biology, Department of Medicine, Taub Institute for Research on Alzheimer's Disease and the Aging Brain, Vagelos College of Physicians & Surgeons, Columbia University, New York, NY, 10032, USA.

[6]Bar-Ilan University, Department of Chemistry, Ramat Gan, 5290002 Israel.

[7]Tokyo Metropolitan University, Tokyo, Japan

[8]BioArctic, Stockholm, SE-112 51 Sweden

[9]Department of Hematology & Oncology, Icahn School of Medicine at Mount Sinai, New York, NY, 10029, USA.

[10]Department of Pathology, Uniformed Services University of Health Sciences, Bethesda, MD, 20814, USA.

[11]Henry M. Jackson Foundation for the Advancement of Military Medicine Inc, Bethesda, MD, 20817, USA.

[12]Department of Medicine, Memorial Sloan Kettering Cancer Center, New York, NY, 10065, USA

[13]Department of Molecular Biology and Biochemistry, University of California, Irvine, CA, 92697, USA.

[14]Center for Dementia Research, The Nathan S. Kline Institute for Psychiatric Research, 140 Old Orangeburg Road, Orangeburg, NY, 10962, USA, and Departments of Psychiatry, Biochemistry & Molecular Pharmacology, and Neuroscience, New York University Grossman School of Medicine, NYU Langone Medical Center, New York, NY, 10016, USA.

[15]Department of Genetics and Genomic Sciences, Icahn School of Medicine at Mount Sinai, New York, NY, 10029, USA.

[16]Department of Medical Imaging & Radiation Sciences, Université de Sherbrooke, Sherbrooke, Quebec, J1K 2R1, Canada

[17]Department of Chemistry, Université de Montreal, Montreal, Quebec, H3C 3J7, Canada

[18]Department of Psychiatry & Alzheimer's Disease Research Center, Icahn School of Medicine at Mount Sinai, New York, NY, 10029, USA.

[19]James J Peters VA Medical Center, Bronx, NY, 10468, USA.

[20]Department of Pediatrics, Icahn School of Medicine at Mount Sinai, New York, NY, 10029, USA.

† Contributed equally to supervision
* Correspondence: michelle.ehrlich@mssm.edu or samuel.gandy@mssm.edu

Michelle E. Ehrlich, M.D.
Professor of Neurology, Pediatrics, Genetics, and Genomic Medicine
Sam Gandy, M.D., Ph.D.
Professor of Neurology and Psychiatry
Icahn School of Medicine at Mount Sinai
Once Gustave L. Levy Place
Box 1138
New York NY 10029

Structured Abstract (150 words)

Background

APP^{E693Q} ("Dutch") transgenic mice develop aging-related learning deficits and accumulate endogenously generated nonfibrillar aggregates of Aβ (NFA-Aβ) and APP α-carboxy terminal fragments. NFA-Aβ correlates with synaptic loss and memory deficits more closely than does fibrillar Aß.

Methods

We assessed the physiological, transcriptomic, ultrastructural, histological, and metabolic changes associated with the accumulation of NFA of Dutch Aβ in brains of *APP*^{E693Q} mice.

Results

Aging-related accumulation of NFA-Aβ in *APP*^{E693Q} mice was revealed by A11 immunohistochemistry and cyclic D,L-α-peptide-FITC microscopy. Presynaptic termini of *APP*^{E693Q} mice developed physiological abnormalities in post-tetanic potentiation, synaptic fatigue, synaptic vesicle replenishment, and an aging-related reduction in mitochondrial complex I activity. Single-cell RNA sequencing showed that excitatory neurons exhibited an altered transcriptomic profile involving "protein translation" and "oxidative phosphorylation".

Discussion

Accumulation of NFA-Aß alters neuronal metabolism but does not activate inflammation. Depletion of all forms of Aβ may be required to eliminate Aβ toxicity with anti-amyloid antibodies.

62 **<u>Introduction</u> (628 words)**

63 Synaptic dysfunction is believed to be a key pathological hallmark of Alzheimer's disease (AD) that begins
64 gradually and parallels clinical cognitive decline (*1-4*). Many studies have demonstrated that the burden of fibrillar
65 amyloid-β (Aβ) proteinopathy does not correlate with synaptic loss (*5-7*) or with cognitive status (*8*). Instead,
66 some investigators have proposed that brain levels of synaptotoxic nonfibrillar aggregates of Aβ (NFA-Aβ)
67 including Aβ oligomers and protofibrils correlate more closely with synaptic loss (*9, 10*). Synaptic NFA-Aβ has
68 been detected in AD brains, and NFA-Aβ levels in human brain synaptosomes can differentiate subjects with early
69 AD from cognitively intact controls with AD pathology (*11-13*). *In vitro*, synthetic NFA-Aβ peptides can cause
70 inhibition of long-term potentiation (LTP) in hippocampal slices (*14, 15*), while *in vivo* injections of NFA-Aβ into
71 the cerebral ventricles of healthy rats leads to cognitive deficits (*16*). Studies using a transgenic mouse model of
72 AD have demonstrated that neuronal loss in the hippocampus correlates with NFA-Aβ levels but not with amyloid
73 plaque burden (*17*). In 2010, we reported a transgenic mouse model overexpressing Dutch mutant human amyloid
74 precursor protein (APP^{E693Q}) on the pan-neuronal Thy1 promoter (*18-25*). This mutation within the Aβ domain
75 substitutes a glutamine for glutamic acid residue, thereby disrupting fibril assembly and favoring the formation
76 of NFA-Aβ. The APP^{E693Q} mutation causes hereditary cerebral hemorrhage with amyloidosis - Dutch type
77 (HCHWAD) (*19*). The neuropathology of HCHWAD shows prominent cerebrovascular amyloidosis and
78 hemorrhage as well as diffuse parenchymal Aβ deposition (*20*). Although the APP^{E693Q} (or "Dutch") transgenic
79 mouse failed to recapitulate the full neuropathology of either AD or HCHWAD, we were struck by the aging-
80 related development of learning behavior impairment that was observed in the absence of detectable fibrillar Aβ.
81 Analysis of the Dutch mouse brain revealed that this learning behavior impairment was directly related to the
82 brain levels of NFA-Aβ (*18, 21*), an observation supported by imaging data in the current paper using epitomic
83 histochemistry with anti-prefibrillar oligomer-specific antibody A11 (*26*) and NFA-Aβ-detecting cyclic peptide-
84 FITC fluorescence microscopy (*22*). The Dutch mice also exhibit detectable cerebrovascular Aβ deposition and
85 traces of perivascular iron (presumably due to the extravasation of red blood cells) without overt hemorrhage.

86 Differential exon usage was also prominent in the Dutch mouse entorhinal cortex and the PSAPP
87 ($APP^{KM670/671NL}/PSEN1^{\Delta exon9}$) mouse dentate gyrus. The transcriptomes from the entorhinal cortex and the dentate
88 gyrus of Dutch mice were also enriched in markers of glutamatergic neurons, synaptic transmission, and protein
89 translation. To study transcriptomics in the Dutch mouse hippocampus, single-cell RNA sequencing (scRNA-seq)
90 was employed and revealed dysregulation of pathways for protein translation, oxidative phosphorylation, and the
91 electron transport chain. Direct measurements of electron transport chain function revealed changes in activity of
92 mitochondrial complex I but not in that of complexes II, III, or IV.

93 In summary, a multi-disciplinary analysis of the Dutch mouse has now revealed alterations in synaptic
94 physiology, gene expression, and protein translation in excitatory neurons, as well as changes in the transcriptomic

95 profile and mitochondrial morphology and activity. Moreover, the high sensitivity of scRNA-seq has enabled
96 neuroinflammation to be ruled out as a major contributor to pathogenesis in the hippocampi of Dutch mice. The
97 present studies are among few focusing on endogenous generation of NFA-Aβ without the concurrent presence
98 of potential confounds from either Aβ fibrils or synthetic peptides. These findings support the notion that fibrillar
99 Aβ is not necessary for the aging-related learning deficit observed in Dutch mice. These data may have important
00 implications for the genesis of cognitive impairment in humans. The clinical response to anti-amyloid antibody
01 therapy may be dampened due to the persistence of toxic NFA-Aβ conformers that go undetected in contemporary
02 analysis of fluid biomarkers and in amyloid fibril positron emission tomography (PET) imaging. Depletion or
03 neutralization of NFA-Aβ may be required for complete elimination of clinically relevant Aβ toxicity.
04

05 **Materials and Methods**

06 *Experimental animals*

07 Male and female 2- to 24-month-old mice were used in this study. All animals were group housed in
08 microisolator cages under a 24-hour light/dark cycle and given *ad libitum* access to food and water. The Dutch
09 mice used in the study express the human *APP* gene harboring the Dutch mutation (APP^{E693Q}) under control of
10 the *Thy1* promoter (*18*). All animal procedures were conducted in accordance with the National Institute of Health
11 Guidelines for the Care and Use of Experimental Animals and were approved by the Institutional Animal Care
12 and Use Committees at the Icahn School of Medicine at Mount Sinai LA10-00462.

13 *Dot blot assay*

14 The cerebral cortices of mouse brain samples were thawed and lysed by adding 2x volume of lysis buffer
15 [5.0 mM NaCl, 5.0 mM EDTA, 1.0 mM dithiothreitol (DTT), and protease inhibitor mixture in 25 mM Tris
16 buffer, pH 7.5] containing 0.5 mm Zirconium Oxide Beads (ADV-ZrOBO5, ORNAT, Israel), homogenized with
17 a tissue grinder motor pestle (Alex-Red, Israel) on ice, and the mixtures were centrifuged at 4°C at 14,000 rpm
18 for 15 minutes. The total protein in each sample was quantified by Nano-Drop absorbance quantification at 280
19 nm.

20 For dot-blot analysis, equal amounts of samples of diluted proteins (100 ng/μL) were directly applied in
21 duplicate onto nitrocellulose membrane and dried at room temperature for 30 minutes. The membrane was then
22 blocked with 5% bovine serum albumin (BSA) in tris-buffered saline (TBS) (pH 7.4) containing 0.1% (v/v) Tween
23 20 (TBST). Blots were incubated overnight at 4°C with: 6E10 mouse monoclonal antibody (1:1000); rabbit
24 polyclonal antibody recognizing prefibrillar oligomers, A11 (1:5000); rabbit monoclonal antibody OC
25 recognizing fibrillar oligomers (1:1000); anti-murine-α-tubulin antibody (1:5000) in TBST containing 5% BSA
26 (all antibodies used are listed in **Supplementary Table 1**). The membranes were washed with TBST three times

and incubated for 1 hour at room temperature with horseradish peroxidase (HRP) conjugated either to an anti-mouse IgG (1:10000) or anti-rabbit IgG (1:5000) in 5% BSA in TBST. The blots were washed with TBST and developed using the enhanced chemiluminescence (ECL) reagent kit (Pierce) in Amersham Imager 680 machine. Images were then used to analyze the mean of integrated densities of each blot using ImageJ software (National Institutes of Health, USA) (*27*).

Immunohistochemistry (IHC) and CP-2-FITC incubation

All staining was performed in paraformaldehyde (PFA)-fixed 30 μm thick sections of Dutch and wildtype mouse brains. For A11 immunohistochemistry and cyclic D,L-α-peptide-2 (CP-2)-FITC fluorescence, free-floating sections were washed with 0.1 M phosphate buffer saline (PBS) in 0.1% Triton (PBST) three times for 15 minutes and blocked with 2% bovine serum albumin (BSA) for 1 hour. Sections were incubated with a rabbit polyclonal antibody A11, recognizing Aβ prefibrillar oligomers (1:2500) in antibody buffer (PBST containing 2% BSA) overnight at 4°C. Sections were washed and incubated with Alexa Fluor 680 secondary goat anti-rabbit antibody (1:1000 Abcam) in antibody buffer for 1 hour at room temperature. Sections were then incubated with fluorescein-5-isothiocyanate (FITC)-conjugated CP-2 [0.15 mg/mL in 2% dimethyl sulfoxide (DMSO)] for 3 hours at room temperature. Sections were washed for 10 min in 1% PBST and kept for 15 min to dry. Sections were then mounted on super frost glass slides, embedded with Fluro-Gel II mounting medium containing DAPI (4',6-diamidino-2-phenylindole dihydrochloride) (Electron Microscopy Sciences, Hatfield PA), cover-slipped, and stored in the dark for microscopic imaging. Immunofluorescence images containing the hippocampus, cortex, and thalamus were obtained using the 20x objective of a Leica DM6000 microscope (Leica Microsystems, Wetzlar, Germany), coupled to a controller module and a high sensitivity 3CCD video camera system (MBF Biosciences, VT) and an Intel Xeon workstation (Intel). All images were analyzed by the Image J program (*27*), and one section from each mouse (from a total of 5 mice in each group) were taken for analysis. The average intensity was calculated from the area of the hippocampus, cortex, and thalamus.

Brain tissue homogenization and Aβ ELISAs

Fresh frozen brain tissue (cerebrum) was homogenized at a 1:5 tissue:buffer ratio, using a Precellys Evolution homogenizer (Bertin Technologies**,** Montigny-Le-Bretonneux, France) to sequentially extract TBS, TBS with 0.5% Triton X-100 (TBS-T) and formic acid (FA) soluble fractions of Aβ. After homogenization in TBS, samples were centrifuged at 16,000× *g* for 1 h at 4 °C (TBS_{16K}). For a subset of experiments, a fraction of this supernatant was further centrifuged at 100,000× *g* followed by collection of the supernatant (TBS_{100K}). Homogenization of the remaining tissue pellet was repeated according to the same procedure with TBS-T, then followed by FA. Brain extracts were analyzed with Aβ1-40 and Aβ1-42 ELISAs, as previously described (*28*). In brief, 96-well half-area plates were coated over night with 50 ng/well of anti-Aβ40 (custom production, Agrisera) or anti-Aβ42 (700254,

60 Thermo Fisher Scientific, USA), then blocked with 1% BSA in PBS for 3 h at RT. TBS_{16K}, TBS-T and FA brain
61 extracts were diluted in ELISA incubation buffer (PBS, 0.1% BSA, 0.05% Tween) and incubated over night at 4
62 °C, followed by detection with 0.5 µg/ml biotinylated 3D6 and HRP-conjugated streptavidin (Mabtech AB,
63 Nacka, Sweden). Signals were developed with K Blue Aqueous TMB substrate (Neogen Corp., Lexington, KA,
64 US). Plates were developed and read with a spectrophotometer at 450 nm. The TBS and TBS-T extracts were also
65 analyzed for soluble Aβ aggregates using two different sandwich ELISAs. The first, based on 3D6 as both capture
66 and detection antibody, allows for detection of Aβ aggregates from the size of a dimer, but not for monomeric Aβ.
67 The second preferentially detects larger soluble Aβ aggregates as it utilizes the Aβ protofibril selective antibody
68 mAb158 for capture and 3D6 for detection (*29*). Ninety-six-well half-area plates were coated over night with 3D6
69 (50 ng/well) and blocked with 1% BSA in PBS for 3 h at RT. Brain extracts were diluted in ELISA incubation
70 buffer (PBS, 0.1% BSA, 0.05% Tween) and incubated over night at 4 °C, followed by 3D6 biotin detection and
71 development as above.

72 *Slice preparation, electrophysiological recordings, and analysis*

73 For electrophysiological experiments, hippocampi from 7- to 13-month-old Dutch and wildtype mice were
74 excised on ice and coronal hippocampal slices (400 µm) were cut with a tissue chopper. Slices were transferred
75 to a recording chamber where they were allowed to recover for 2 hours at 29°C and perfused with artificial
76 cerebrospinal fluid (ACSF) containing (124.0 mM), KCl (4.4 mM), Na_2HPO_4 (1.0 mM), $NaHCO_3$ (25.0 mM),
77 $CaCl_2$ (2.0 mM), $MgCl_2$ (2.0 mM), and glucose (10.0 mM). ACSF was bubbled with carbogen (95% O_2 and 5%
78 CO_2) and perfused at a flow rate of 2 ml/minute.

79 Field excitatory post-synaptic potentials (fEPSP) were measured after stimulating the Schaffer collateral fibers
80 with a bipolar tungsten electrode placed at the CA3 and recording at the *stratum radiatum* of CA1 with a glass
81 pipette filled with ACSF. Basal synaptic transmission was evaluated by plotting the relationship between increased
82 voltages (5 V to 35 V) and evoked fEPSP responses, generating an input-output (I-O) curve. Recordings were
83 measured at approximately 35% of the maximum evoked response as determined by the I-O curve. For LTP
84 recordings, a 30-minute baseline was recorded prior to theta-burst stimulation (4 pulses at 100 Hz, with the bursts
85 repeated at 5 Hz and 3 tetani of 10-burst trains administered at 15-second intervals), responses were recorded for
86 2 hours after tetanization and measured as fEPSP slope expressed as percentage of baseline. Paired-pulse
87 facilitation (PPF) was induced by pairing two pulses at intervals of 15, 20, 30, 40, 50, 100, 200, 300, 500 and
88 1000 ms. PPF was expressed as the ratio between the second and the first fEPSP slopes. Post-tetanic potentiation
89 (PTP) was induced by the above-described theta-burst stimulation protocol in presence of the NMDA receptor
90 blocker D-APV (50 µM). Synaptic fatigue (SF) and replenishment were measured by 100 Hz stimulation followed
91 by 7 stimuli spaced at 125 msec from each other in the presence of D-APV (50 µM).

Results were analyzed in pClamp 11 (Molecular Devices) and fEPSP slopes were compared by 2-way ANOVA for repeated measures for the I-O curve, LTP, PPF and PTP recordings. For statistical comparison of synaptic fatigue and replenishment, the rates of exponential growth/decay (k) extra sum-of-squares F test was used to test whether k differed between data sets vs. the data sets sharing one k-value. Statistics were performed using GraphPad Prism 9 software. Data were expressed as mean ± SEM. The level of significance was set at $p<0.05$.

Perfusions and tissue processing for electron microscopy and array tomography

For electron microscopy (EM) and array tomography synapse studies, 12-month-old Dutch and wildtype mice were anesthetized intraperitoneally, and transcardially perfused with 1% PFA in phosphate-buffered saline (PBS; pH 7.4) followed by 4% PFA with 0.125% glutaraldehyde in PBS as described previously (*24, 30, 31*). The brains were carefully removed, hemisected, postfixed overnight at 4°C in 4% PFA in PBS with 0.125% glutaraldehyde for synapse and immunogold analyses, or by 2% PFA with 2% glutaraldehyde in PBS for presynaptic vesicle analysis, and sectioned on a Vibratome (Leica VT1000S, Bannockburn, IL) into 250-µm thick sections. All sections were stored at 4°C in PBS with 0.1% sodium azide until use. Coronal sections encompassing the CA1 region of the hippocampus were prepared for EM as reported (*24, 31*). For synapse and immunogold analyses, slices were cryoprotected in graded phosphate buffer/glycerol washes at 4°C, and manually microdissected to obtain blocks containing the CA1 region. The blocks were rapidly freeze-plunged into liquid propane cooled by liquid nitrogen (-190°C) in a Universal cryofixation System KF80 (Reichert-Jung) and subsequently immersed in 1.5% uranyl acetate dissolved in anhydrous methanol at -90°C for 24 hours in a cryosubstitution unit (Leica). Block temperatures were raised from -90°C to -45°C in steps of 4°C/hour, washed with anhydrous methanol, and infiltrated with Lowicryl resin (Electron Microscopy Sciences) at -45°C. The resin was polymerized by exposure to ultraviolet light (360 nm) for 48 hours at -45°C followed by 24 hours at 0°C. For presynaptic vesicle studies, tissue blocks were washed overnight in 0.1 M sodium cacodylate buffer, placed in 1% tannic acid/0.1 M cacodylate buffer solution at room temperature for one hour and washed 3 times for 10 minutes each in 0.1 M sodium cacodylate. The samples were then incubated for 1 hour at room temperature in 2% osmium tetroxide/double distilled water (ddH_2O), washed again in 0.1 M sodium cacodylate 3 times for 10 minutes then subjected to a graduated ethanol dehydration series. After dehydration, the tissue samples were infiltrated with Spurr Low Viscosity Embedding Kit (Sigma Aldrich) and polymerized for 12 hours at 70°C. For both EM preparations, block faces were trimmed, ultrathin sections (90 nm) were cut with a diamond knife (Diatome) on an ultramicrotome (Reichert-Jung), and sections were collected on formvar/carbon-coated nickel slot grids (Electron Microscopy Sciences).

Post-embedding immunogold labeling for EM

Immuno-gold labeling was performed using a previously optimized method (*32*). Briefly, the EM sections were treated with 0.1% sodium borohydride in 50 mM glycine prepared in Tris buffer for 6 minutes in the dark, to remove aldehydes. Sections were then subjected to six quick rinses and two 10-minute washes in TBS. The sections were incubated for 30 min in blocking buffer consisting of 2% human serum albumin (HSA) in TBS with 0.1% Triton X-100. After three short washes in TBS, the sections were incubated in anti-glutamate receptor 2 & 3 rabbit polyclonal antibody (Millipore AB1506, diluted 1:100 in 2% HSA in TBS) at room temperature overnight with gentle shaking. Following six quick rinses and two 5-minute washes in TBS, the grids were incubated in blocking buffer for 20 minutes, washed three times, and incubated for 90 minutes at room temperature in goat anti-rabbit IgG conjugated to 10-nm gold particles (Aurion 25362), diluted 1:40 in 2% HSA and 5 mg/ml polyethylene glycol in TBS. The grids were rinsed six times and washed for 5 minutes in TBS and then in deionized water. Imaging was done using an H-7000 electron microscope (Hitachi High Technologies America, Inc.) with an AMT Advantage CCD camera (Advanced Microscopy Techniques) at 15,000x. The electron micrographs were adjusted for brightness and sharpness with Photoshop CS5 (Adobe Systems).

Quantifying synapse density, ultrastructure, and distribution of immunogold particles at mGluR-2/3-labeled synapses

All EM analyses were conducted by an experimenter blinded to the genotypes of the mice. For synapse quantification and ultrastructural analysis, nine sets of serial images across the same set of 5 consecutive ultrathin sections were taken from the *stratum radiatum* of CA1 and imported into Adobe Photoshop (version CS5). To obtain a stereologically unbiased population of synapses for quantitative morphologic analysis, we used a disector approach on ultrathin sections as described (*24, 30, 31, 33*). Briefly, all axospinous synapses were identified within the first and last 2 images of each 5-section serial set and counted if they were contained in the reference image (layers 1 and 4) but not in the corresponding look-up image (layers 2 and 5). To increase sampling efficiency, the reference image and look-up image were then reversed; thus, each animal included in the current study contributed synapse density data from a total of 18 disector pairs. The total volume examined was 11.317 μm^3, and the height of the disector was 180 nm. Axospinous synapse density (per μm^3) was calculated as the total number of counted synapses from both images divided by the total volume of the disector. The criteria for inclusion as an axospinous synapse included the presence of synaptic vesicles in the presynaptic terminal and a distinct asymmetric PSD separated by a clear synaptic cleft. For a synapse to be scored as perforated it had to display two or more separate PSDs.

To measure structural parameters such as spine head diameter and PSD length, we identified all axospinous synapses in the middle portion of three serial sections. The synapse and spine head were followed through layers

2-5. In each layer, the PSD length (if present) and the spine head diameter at its widest point parallel to the synapse were measured. PSD area was determined by summing the PSD lengths through all sections and multiplying by section thickness (90 μm). This same process was repeated for unique synapses in layer 4 (reference layer 5), following the synapses from layer 4 to layer 1. Each of these synapses were also classified as non-perforated or perforated. A total of 734 total synapses (341 from Dutch mice and 393 from wildtype) were analyzed in this manner. An average of 81 synapses per animal and a minimum of 71 synapses per animal were sampled. For each unique synapse in layer 2 in each series (as identified for PSD length and spine head analysis above), the synapse was followed through layers 2 though 5 and the number of immunogold particles in each of the following areas were counted: active zone (presynaptic, within 45 nm of the membrane across from the PSD; region A), synaptic cleft (region B), PSD (region C), peri-synaptic (peri—PSD, within 200 nm of the PSD on the post-synaptic spine head; region D), postsynaptic membrane (>200 nm away from the PSD; region E), and postsynaptic cytoplasm (region F). A cutoff of 45 nm away from the membrane was used to differentiate between receptors at the membrane and receptors in the cytosol.

For presynaptic vesicle analysis, 100 synapses per animal were analyzed from at least 30 different images taken at a magnification of 8,000x. PSD length, maximum spine head diameter, and cytosolic area of the presynaptic terminal were measured using Adobe Photoshop 2023. Vesicles in the presynaptic terminal were labeled with a dot in the center of the vesicle, and a line was drawn over the PSD. An algorithm was written in Python that measured the shortest distance between each vesicle (represented by the dot in the center) and its corresponding PSD (represented by the manually drawn line over the PSD) and reported a list of measurements for all vesicles within an adjustable threshold distance. For each synapse, the total number of vesicles was determined with output from this algorithm, along with their individual distances from the PSD. The vesicles were divided into bins of 10 and 50 nm for comparison of spatial distribution within the presynaptic terminal. Additionally, vesicles within 10 nm of the PSD were classified as docked, based on a 17 nm average minimum diameter of vesicles in our samples (*34-36*).

scRNA-seq and data analysis

For the scRNA-seq experiments, fresh hippocampi were dissected from 12- to 13-month-old Dutch and wildtype mice, and the tissue was dissociated into a single-cell suspension following the 10X Genomics sample preparation protocol. We pooled the hippocampi from 3 mice of the same gender, genotype, and age to reach the target concentration of 2000 cells/μl. The single cell cDNA libraries were generated using a V3 Chromium kit (10X Genomics) and sequenced using a NovaSeq S4 (Illumina).

The raw sequencing data were processed using the standard Cell Ranger pipeline to generate unique molecular identifier (UMI) count matrices. Starting from UMI matrices, we first performed quality control (QC) by removing

89 low-quality cells with either too few (< 200) or too many (> 4000) genes detected, retaining 61,642 cells after
90 filtering. We then removed insufficiently detected genes by keeping 20,548 genes expressed in more than one cell.
91 After QC, we obtained 5,266 ~ 10,949 cells per individual, and an average of 618 unique genes per cell per
92 individual. We performed a clustering analysis using a well-established scRNA-seq data integration workflow
93 based on R package Seurat (v3) (*37*). Briefly, the UMIs data were first normalized by sequencing depth and log-
94 transformed using the LogNormalize method implemented in Seurat. The 2,000 most variable gene features were
95 identified, scaled, and centered. The scRNA-seq data across all sequencing libraries were combined based on the
96 canonical correlation analysis (CCA) integration method available from Seurat. Next, dimensional reduction was
97 performed using principal component analysis (PCA) based on the 2,000 most variable genes. The top 25 principal
98 components (PCs) collectively explaining more than 90% of the variance were selected for calculating 2D
99 dimensional reductions by Uniform Manifold Approximation and Projection for Dimension Reduction (UMAP)
00 (*38*). The same top 25 PCs were also used to compute the nearest neighbor graph and the subsequent cell clusters
01 with the Louvain algorithm implemented in Seurat (*37*). This clustering analysis resulted in 14 clusters (named
02 as Clusters 0 – 13, sorted by cluster size in a decreasing order) at a clustering resolution of 0.1. These clusters
03 contained 267 to 20,702 cells each.
04
05 *Cluster cell type annotation*
06 For each cluster, we first interrogated the expression patterns of known gene markers to annotate clusters into
07 major cell-types: inhibitory neurons (*Gad1*, *Gad2*), excitatory neurons (*Slc17a7*), astrocytes (*Aqp4*),
08 oligodendrocytes (*Mog*), microglia (*Csf1r*, *Tyrobp,* and *Trem2*), oligodendrocyte progenitor cells (*Vcan* and
09 *Pdgfra*), endothelial cells (*Flt1*), and pericytes (*Vtn* and *Pdgfrb*). Next, we calculated *de novo* cluster signatures
10 by comparing the cells in a cluster against the cells of the other clusters using Wilcoxon rank sum test in Seurat.
11 We defined cluster marker genes as those upregulated by at least 1.2-fold and with Bonferroni adjusted p-value
12 less than 0.05. To assist the annotation of cell type of each cluster, we overlapped the *de novo* cluster marker gene
13 signatures with a large-scale collection of cell type markers curated from over 1,054 single-cell experiments (*39*),
14 with p-value significance of the overlaps computed by a hypergeometric test.
15
16 *Cluster-specific differential gene expression and functional enrichment analysis*
17 DEGs between Dutch and wild type sample groups in each cluster were identified using MAST (*37, 40*)
18 implemented in Seurat. Similarly, DEGs between males and females, and DEGs between Dutch and wild type in
19 each sex group were identified using MAST. DEGs were determined at the cutoff of Bonferroni-corrected p-value
20 ≤ 0.05. Functional enrichment of DEGs with MSigDB gene annotation collections was examined by a

hypergeometric test. Results with Benjamini-Hochberg (BH) correction p-value ≤ 0.05 were considered statistically significant.

Microglia subclustering analysis

We studied a subset of microglial cells from the full data matrix. PCA was performed and then the top PCs collectively explaining more than 90% of the variance were selected for calculating dimensional reduction by UMAP (*38*) as well as for clustering analysis using Seurat (*37*). To test if the microglia subclusters represent known subtypes, we computed single cell signature scores (*41*) corresponding to homeostatic, disease-associated microglia (DAM), type I IFN-induced (IFN) and MHC-expressing (MHC) microglia based on signature genes curated by Chen and Colonna *(42)*.

Quantifying presynaptic mitochondrial numbers and morphology

For analysis of mitochondria, 12 series of 9 consecutive 90-nm thick sections were selected from each mouse using a systematic-random approach for EM imaging. All mitochondrial analyses were performed by the same experimenter, blinded to the group designation of subjects as described (*43*). For each series of 9 consecutive sections, the middle fifth section was used as a reference, and all pre-synaptic axonal boutons containing a mitochondrion were identified. Each of these boutons was followed throughout the series, and the number, length and morphology of mitochondria were recorded. Mitochondria were classified as either straight or curved. Mitochondria that were bent at least 90° were identified as curved, while all other mitochondria were classified as straight.

Statistics

Data sets from the dot blot assays were analyzed using a one-way ANOVA followed by Tukey's multiple comparisons test. Data sets from the A11 immunohistochemistry and CP-2 cyclic peptide-FITC (CP-2-FITC) (*22*) fluorescence microscopy were analyzed using a two-way ANOVA followed by Sidak's multiple comparisons test. Data sets were analyzed using a two-tailed Student's t-test. Threshold for significance was set at $\alpha = 0.05$. Distribution of mGluR-2/3 immunogold particles was analyzed using repeated measures ANOVA. Data are represented as mean ± SD. Statistical analyses were carried out using Prism software (version 9.2.0, GraphPad Software, San Diego, CA).

Data Availability

The scRNA-seq data (cell ranger processed count matrices) are in a Synapse repository (accession syn52752404, with direct link https://www.synapse.org/#!Synapse:syn52752404/files/).

53 **Results**

54

55 ***Dutch mice show increased levels of nonfibrillar aggregates with aging.***

56 Aging-dependent investigation of the Dutch mice revealed that 12 months is the first age at which deficits
57 attributable to NFA-Aβ can be detected (*18*). To determine the involvement of NFA-Aβ in brain changes, multiple
58 analyses were conducted at different ages, before and after the appearance of NFA-Aβ. Epitomic characterization
59 was performed on cortical tissue from 2- and 24-month-old Dutch mice. Interestingly, this characterization
60 revealed a significant increase with aging in the A11/6E10 ratio (ratio of prefibrillar oligomer content to total Aβ
61 content; $F(3,16) = 17.05$; $p < 0.0001$), but no such aging-related change in the OC/6E10 ratio (ratio of fibrillar oligomer
62 content to total Aβ content; $F(3,16) = 2.557$; $p = 0.0916$) in Dutch mice (**Figure 1, Supplementary Figure 1**).
63 Furthermore, brains were analyzed for the presence of protofibrils (PF) using the homogenization protocol
64 described in Tucker *et al.* (*44*) and assayed for PF levels in the TBS soluble fraction using a mAb158-mAb158
65 sandwich MSD assay employing an in-house synthetic protofibril as calibrator. Both assays showed very low
66 levels of Aβ PF. In the mAb158 sandwich assay, Aβ PF levels were around 100 pM, levels indistinguishable from
67 those in homogenates of wildtype mice (**Supplementary Figure 1**). No PF were detected in the cerebellum.
68 Levels of PF in Dutch mice were approximately 10- to 100-fold lower than those measured in Tg-APP^{ArcSwe} and
69 Tg2576 (depending on age analyzed). In addition, $A\beta_{38/40/42}$ fragments were analyzed in the TBS insoluble pellet
70 fraction after dissolution in formic acid and neutralization. Levels of Aβ PF were again very low, consistent with
71 the absence of parenchymal plaques in Dutch mice.

72 The elevation of NFA-Aβ levels in the cortex, thalamus, and hippocampus of Dutch mice was visually and
73 morphologically confirmed using a combination of immunohistochemistry using A11 antibody and fluorescence
74 microscopy employing cyclic D,L-α-peptide-2 (CP-2)-FITC as a fluorescein-tagged NFA-Aβ-detecting ligand
75 (*22*) (**Figure 1, Supplementary Figures 1-3**). The hypothesis that CP-2 and A11 bind to similar or identical
76 domains on NFA-Aβ was confirmed by cross-competition blocking experiments in which pre-incubation of brain
77 slices with CP-2 peptide prevented the subsequent binding of the prefibrillar oligomer-specific antibody A11
78 (**Supplementary Figure 4**). Furthermore, the interaction of CP-2 with NFA-Aβ has been characterized (*45-49*):
79 CP-2 was demonstrated (1) to stabilize Aβ dimers and trimers using a photoinduced cross-linking of unmodified
80 proteins (PICUP) assay (*45-48*) and (2) to bind 10 nm particles typical of NFA-Aβ (*49*). In the current study, CP-
81 2 exhibited similar K_d values for both fibrillar and nonfibrillar forms of Aβ in surface plasmon resonance (SPR)
82 assays (**Supplementary Methods**): CP-2 interacted with Aβ fibrils and NFA-Aβ with K_d values of 6 and 4 μM,
83 respectively.

84 As shown in **Supplementary Table 2**, there were no important male-female differences in the levels of NFA
85 Aβ in either Dutch or Dutch PS1 mice. Among the neurophysiological data, the differences in replenishment
86 were statistically significant regardless of whether they were analyzed by sex or whether data from different sexes
87 were pooled for analysis. For fatigue and PTP analyses, only one sex was significant, but this was probably
88 because of the disparity of sample sizes rather than a sex-specific effect. There were insufficient numbers of
89 individual sexes studied by EM to calculate sex-specific mitochondrial size reliably.
90
91 ***Dutch mice showed no significant impairment in basal synaptic transmission and long-term synaptic***
92 ***plasticity in the hippocampus.***
93 The relationship between synaptic input strength and the resulting electrical response, the so-called "input-
94 output relation" and long-term potentiation (LTP) were tested in 7- to 7.5-month-old and 10.5- to 11-month-old
95 Dutch mice. The two genotypes displayed similar input-output relationships and LTP in both age groups,
96 suggesting that basal synaptic transmission at the CA1 region of the hippocampus and long-term synaptic
97 plasticity at the Schaffer collateral pathway were unimpaired in Dutch mice **(Figure 2A, 2B, 2C, 2D**).
98
99 ***Dutch mice exhibited defects in PTP, SF, and replenishment of the vesicle pool after depletion.***
00 We assessed several mechanisms related to function of the presynaptic terminal. Both 11- to 13-month-old
01 Dutch mice and their wildtype littermates showed the same response in paired-pulse facilitation (PPF) **(Figure**
02 **2E)**, a type of short-term plasticity that is most likely dependent upon the build-up of Ca^{2+} in the presynaptic
03 neuron due to the close pairing of two action potentials. Accumulation of Ca^{2+} in the presynaptic neuron results
04 in increased neurotransmitter release and subsequently increased response after the arrival of the second action
05 potential (*50*). Accordingly, facilitation is no longer present when a long-time interval (1 second) is introduced
06 between the two stimuli. Both wildtype and Dutch mice showed increased facilitation at short time intervals, and
07 no difference was observed between the two genotypes. In contrast to PPF, Dutch mice showed decreased post-
08 tetanic potentiation (PTP) compared to wildtype mice **(Figure 2F)**. PTP is performed in the presence of D-2-
09 amino-5-phosphonovalerate (D-APV) that blocks NMDA receptors, thereby preventing the onset of NMDA-
10 dependent postsynaptic mechanisms that might interfere with measurement of plasticity. Due to the DAPV, the
11 fEPSP slope declines back to baseline a few seconds after stimulation. PTP is another form of short-term plasticity
12 and reflects the enhanced release of neurotransmitter due to the increased levels of Ca^{2+} at the presynaptic terminal
13 during the tetanic stimulation (*51*).
14 We also studied the effect of the Dutch mutation on the efficacy of presynaptic mechanisms by examining
15 synaptic fatigue (SF) and replenishment, after depletion, of the vesicle pool. Both mechanisms appeared to differ
16 between wildtype and Dutch mice. Specifically, the SF showed a faster rate of decay (**Figure 2G**) and the

replenishment phase had a higher growth rate in the Dutch compared to wildtype mice (**Figure 2H**). The decline in the slope that is observed during SF is thought to represent the depletion of the readily releasable pool (RRP) of neurotransmitter that resides in vesicles at the presynaptic cells. Replenishment after depletion with high frequency stimulation depicts the refilling process of the RRP. Mechanistically, both SF and replenishment have been suggested to depend on accumulation of residual Ca^{2+} at the presynaptic terminal (*50, 51*).

Dutch mice had larger PSD area on small mGluR-2/3^{+} synapses in the CA1 region.

Changes in mGluR-2/3^{+} excitatory neurons were examined at the ultrastructural level in 12-month-old mice. Comparable percentages of mGluR-2/3^{+} synapses among total, non-perforated, and perforated synapses in the CA1 were observed in Dutch and wildtype mice using immunogold EM against mGluR-2/3 (**Figure 3A-C**). Moreover, Dutch and wildtype mice exhibited no difference in the total and perforated synapses (**Figure 3D, F**). Higher postsynaptic density (PSD) area of non-perforated mGluR-2/3^{+} synapses was detected in the Dutch compared to wildtype mice (**Figure 3E**), both of which had comparable distributions of mGluR-2/3^{+} particles per PSD area (**Figure 3G-I**).

Dutch mice showed no change of hippocampal mGluR-2/3 expression nor of mGluR-2/3+ synapse density.

Comparable levels of mGluR-2/3 protein were observed in Western blots of the insoluble membrane fraction from the hippocampus of 12-month-old Dutch and wildtype mice (**Supplemental Figure 5A**). Considering that Western blots may not detect regional differences, array tomography and immunofluorescence were used to analyze mGluR-2/3 puncta after staining serial sections of CA1 neurons with Neurotrace (**Supplemental Figure 5B**). Comparable densities in the CA1 of Dutch and wildtype mice were observed in 3D reconstructions of mGluR-2/3 synaptic puncta by array tomography (**Supplemental Figure 5C**, $F_{(4,3)} = 1.476$, $p = 0.7802$). Quantification of the total mGluR-2/3 puncta output yielded an average tissue density (puncta/μm^3) of 0.322 ± 0.112 for Dutch and 0.275 ± 0.087 for wildtype mice. Both genotypes exhibited comparable puncta size ranges, and no significant difference in average mGluR-2/3 puncta size (**Supplemental Figure 5D**; $F_{(1,3)} = 0.751$, $p = 0.538$) per percentile per sample. Similarly, neither the density nor size of GluN1 puncta were altered in Dutch mice (**Supplemental Figure 5E-F**; $F_{(4,3)} = 1.431$, $p = 0.8003$ for density and $F_{(1,3)} = 0.116$, $p = 0.950$ for puncta size).

Dutch mice had no change in synaptic distribution of mGluR-2/3+ in the CA1.

Comparable distributions of mGluR-2/3 were observed by immunogold labeling and electron microscopy (EM) at the synapse (**Supplemental Figures 6A-C**), pre- and postsynaptic compartments (**Supplemental Figure**

6D), presynaptic active zone, synaptic cleft, peri-synaptic area, postsynaptic membrane, and postsynaptic cytoplasm (**Supplemental Figure 6E**) in 12-month-old Dutch and wildtype mice.

Dutch mice exhibited no change in vesicle size nor number of docked vesicles but show a trend towards fewer vesicles in the reserve pool at presynaptic terminals in the CA1.

The size, number, and distribution of vesicles were quantified within the presynaptic terminal of 12-month-old mice. No differences were observed in synaptic vesicle sizes at the presynaptic terminal nor the number of docked vesicles at the synapses of the active zone in Dutch and wildtype mice (**Supplemental Figure 7A-C, E, G**). A decline in the number of synaptic vesicles was found in the reserve pool beyond 300 nm from the active zone of Dutch compared to wildtype mice but did not reach statistical significance and appeared to be driven by vesicles in large synapses (**Supplemental Figures 7D and 7H**). The hippocampi of Dutch and wildtype mice exhibited no differences in the levels of the postsynaptic density protein of 95kDa (PSD95) and of the presynaptic marker synaptophysin (**Supplemental Figure 7I**).

Dutch mice display shared gene expression profiles across multiple cell types.

Employing brains from Dutch mice alongside sex- and age-matched wildtype littermates, scRNA-seq was performed. Hippocampi were collected from mice at 12 months, an age characterized by established cognitive deficits and high levels of NFA-Aβ and α-CTF in Dutch mice (*18*). After quality control filtering (**Supplemental Figure 8**), 61,642 (32,661 Dutch and 28,981 wildtype) cells were isolated from thirteen distinct clusters which were identified based on the expression of well-known cell-type-specific markers (**Figures 4, 5A-B**, **Supplemental Tables 3-4**). Pseudo-bulk differential expression analysis was used to identify gene expression changes within each cell type. For further analysis (C0-6), clusters of interest were identified based on differentially expressed genes (DEGs; adj. p-value cutoff <0.05) (**Figure 5C-D**, **Supplemental Figures 9-12, Supplemental Table 5**).

Faced with considerable overlap in DEGs, the clusterProfiler (*52*) approach was employed to compare biological themes and identify the Gene Ontology (GO) term enrichment shared among the gene clusters. Among the shared terms were "structural constituent of ribosome" (example genes include: *Rpl23, Rpl30, Rpl37a, Rpl6, Rpl9, Rps24*) (**Figure 6A-B**), and "amyloid-beta binding" (*Apoe, Atp1a3, Clu, Cst3)* (**Figure 6A, C**). Across clusters, the shared DEGs and GO terms were similar to a previously identified "aging signature" in 21- to 22-month-old mouse brain (*53*), in which ribosomal protein genes, long noncoding RNA genes (e.g., *Malat1*) as well as ribosome-related pathways and processes, all were significantly affected across multiple cell types compared to that of 2-to 3-month-old counterparts. Across clusters, 453 DEGs were found to overlap with the aging-related

gene list (**Figure 6D**) from which 435 genes displayed the same directionality across all clusters (389 upregulated and 46 downregulated, **Figure 6E**) as reported (*53*).

Dutch mice do not show obvious differences in microglial gene expression.

In many Aβ-depositing mouse models of AD, microglia show prominent transcriptional responses and increased microgliosis with conspicuous peri-plaque localization (*54, 55*). Furthermore, the microglial immune response to NFA-Aβ has been implicated as an early, key step in AD pathogenesis. To investigate the microglial responses in more detail, we performed subclustering analysis, which revealed three subpopulations of microglia in the hippocampus (**Figure 7A**). None of the subpopulations showed higher abundance in either genotype. The subpopulations also did not segregate based on expression of established microglial profile markers, such as homeostatic, disease-associated microglia (DAM) (*56*), type I interferon-induced (IFN), and major histocompatibility complex-expressing (MHC) signatures (*42*) (**Figure 7B**). Expression of homeostatic markers was high in all microglia subpopulations and did not change in microglia from the hippocampus of Dutch mice (**Figure 7C**). In addition, no differences were seen in IBA1 IHC between 12-month-old Dutch and wildtype mice (**Supplemental Figure 13A-B**). We observed an approximately 3-fold increase in co-localization of C1q with synaptic puncta in Dutch mice ($p = 0.0181$, **Supplemental Figure 13C**). These data strengthen the conclusion that C1q–synapse association is significantly elevated in Dutch mice at 12 months of age, as was reported in J20 mice *(57).*

Dutch mice show changes in gene expression associated with translation in excitatory neurons.

Cluster 6 was identified as excitatory neurons and showed the most extensive and unique transcriptional response in Dutch mice (**Figure 6C-D, Figure 7A**). In the GO term analysis, upregulated Cluster 6 DEGs included "cytoplasmic translation" (*Eif2s2, Eef1a1, Eef1b2, Rpl22, Rpl26, Rpl27*) and "negative regulation of amyloid fibril formation" (*Cryab, Pfdn6, Slc25a4, Grin2b, Stmn1, Smad4, Pik3r1*, **Figure 7B, Supplemental Table 6**). Notably, "regulation of synapse organization" was also among the top GO terms (*Cask, Cdh8, Gpc4, Grin2b, Mef2c, Nrxn1, Pafah1b1, Ptprd, Tuba1a, Ube2v2, Malat1, Opa1, Mycbp2, Nrcam, Il1rapl1, Arhgef9*), a selection of which are also highlighted in **Figure 7A**. In the GO term analysis, downregulated Cluster 6 DEGs included those related to processes associated with mitochondrial bioenergetic function: i.e., "electron transport chain" (*Mt-Co1, Mt-Co3, Mt-Cytb, Ppp1cb, Calm2*) and "oxidative phosphorylation" (*mt-Atp6, mt-Nd1, mt-Nd3)* (**Figure 7C, Supplemental Table 7**). A selection of unique DEGs from Cluster 6 is shown in **Figure 7D.**

Gene expression was also examined for biological processes associated with presynaptic mechanisms and synaptic transmission, specifically "regulation of synapse organization", which is a subset of "regulation of cell morphogenesis" (**Supplemental Figure 14A**). Myocyte Enhancer Factor 2C (*Mef2c*) is among this gene list and

has been identified as a candidate risk gene for developing late onset Alzheimer's disease (LOAD) (*58, 59*). Considering that oligodendrocytes can modulate presynaptic properties and synaptic transmission (*60, 61*), relevant biological processes such as "modulation of chemical synaptic transmission" were assessed and found among the top biological processes in Cluster 4 oligodendrocytes (**Supplemental Figure 14B, Supplemental Table 8**). Approximately 25% of the genes present in this biological process are among DEGs in Cluster 6. Genes associated with synaptic transmission that were among those specific to Cluster 4 included transferrin (*Trf,* a recently identified biomarker of AD) (*62*), and carbonic anhydrase 2 (*Car2*). Carbonic anhydrase inhibitors have been considered for prevention of neurovascular dysfunction in CAA and AD due in part to their ability to prevent mitochondrial dysfunction and oxidative stress (*63, 64*).

A cell-cell communication analysis was performed using the software tool Cellphone DB to compute interactions between clusters based on the known Ligand-Receptor (LR) pairs (**Supplemental Table 9**). For each LR in each sample, the software estimated the interaction strength from Cluster 4 oligodendrocytes to Cluster 6 excitatory neurons, from which differences in interaction strengths between Dutch and WT mice were evaluated by t-test. Twelve LR pairs showed significant interaction difference at p-value ≤ 0.05, and all twelve presented higher interactions in Dutch mice. Among these LRs, *Gabbr2* was up-regulated in the Cluster 6 excitatory neurons in Dutch mice compared to those of wildtype (log2FC = 0.19, adj. p-value = 3.6E-4). In Dutch compared to wildtype mice, stronger interactions were exhibited by *Gabbr2* with multiple GABA inhibitory neurotransmitter complex partners including GAD2, SLC6A11, SLC6A1, SLC6A8, SLC6A6, and SLC32A1.

Dutch mice have fewer and smaller mitochondria in CA1 presynaptic boutons.

The number and morphology of mitochondria were assessed in the presynaptic terminals of excitatory neurons in the *stratum radiatum* of Dutch and wildtype mice (**Figure 8A, B**). Previously, NFA-Aβ has been reported to cause imbalance in mitochondrial fission-fusion, leading to fragmented morphology and altered function (*65-69*). Fewer presynaptic mitochondria were found in Dutch compared to wildtype mice (**Figure 8C**, mean ± SD for total of mitochondria per presynaptic bouton = 75.60 ± 14.62 in Dutch and 106.3 ± 20.06 in wildtype, p = 0.0324 by two-tailed unpaired t test). This deficiency in the Dutch mice was likely due to fewer straight mitochondria at the presynaptic terminals, because curved mitochondria numbers were unchanged between genotypes (**Figure 8D-F**, mean ± SD for number of straight mitochondria = 71.80 ± 15.06 in Dutch and 101.3 ± 17.95 in wildtype, p = 0.314 by two-tailed unpaired t test. Mean ± SD for number of curved mitochondria = 3.80 ± 2.59 in Dutch and 5.00 ± 2.16 in wildtype). In assessments of differences in morphology, mitochondrial diameters were comparable (**Figure 8G**, mean ± SD = 301.8 ± 28.73 in Dutch and 328.6 ± 19.29 in wildtype), but shorter lengths were found in 12-month-old Dutch compared to wildtype mice, as estimated from the number of layers traversed

in the consecutive sections by each mitochondrion (**Figure 8H**). Each layer traversed was ~ 80 nm using 3-dimensional reconstruction of measurements from serial sections.

Dutch mice have reduced mitochondrial electron transport chain complex I activity.

The activities of electron transport chain complexes I-IV and citrate synthase were assessed in hippocampi from 7- and 12-month-old wildtype and Dutch mice as described (*70, 71*). Each complex activity was standardized to either μg protein ($p = 0.0355$) or to mU/ml of citrate synthase (CS) and analyzed using an unpaired t test ($p = 0.0197$) (**Supplemental Figure S15, Supplemental Tables 10, 11**). Mitochondrial complex I activity was reduced in 12- but not 7-month-old Dutch compared to that of wildtype mice.

Dutch and Arctic Aβ peptides increase mitochondrial membrane potential in cultured cells.

Both Dutch APP^{E693Q} and Arctic APP^{E693G} are known to form primarily oligomers. We assayed wildtype, Dutch, and Arctic mutant Aβ peptides (**Supplemental Figure S16**) using cultured Neuro2a cells. In this experiment, Neuro2a cells were respectively treated for 24 h with wildtype peptide and Aβ carrying at position 22 either the Dutch E693Q or the Arctic E693G mutation. Cells were then stained with a MT-1 MitoMP detection kit, using a mitochondrial membrane potential-sensitive dye, and MitoTracker Green, which labels total mitochondrial mass. Representative images are presented from one of three independent experiments showing similar results. For quantitative analysis, 30 cells per condition were analyzed. Mitochondrial membrane potential was increased by both oligomerogenic mutant peptides, as reported (*72*). Data were analyzed by one-way ANOVA followed by Dunnett's post hoc test. NS, not significant ($p > 0.05$); ****, $p < 0.001$. Scale bar, 10 μm.

<u>Discussion</u> (1507 words)

The localization of mouse brain Dutch NFA-Aβ was ascertained using immunohistochemistry with A11 antibody and fluorescence microscopy with a cyclic peptide-FITC ligand (*22*). In contrast to the apparently normal density and morphology of synapses in excitatory neurons, we observed abnormalities in the apical dendrite structure in the CA1 of Dutch mice (*24*). Impaired short-term synaptic plasticity developed at the CA1-CA3 synapses first appearing at the age of 11 to 13 months.

Assessment of the I-O curve and the LTP response after high frequency stimulation in the CA1-CA3 synapses, indicated no difference between Dutch and wildtype genotypes. In contrast, intracerebroventricular injection of synthetic Dutch and Arctic (APP^{E693G}) Aβ peptides have been previously reported to block LTP in rats (*73*). Despite normal *long-term* synaptic plasticity in young or old Dutch mice, defects in several types of *short-term*

plasticity emerged in the aging 11- to 13-month-old Dutch mice. Specifically, mice carrying the Dutch mutation exhibited impaired PTP, synaptic fatigue (SF), and impaired replenishment of the synaptic pool, but unaffected PPF. Both PPF and PTP are related to accumulation of Ca^{2+} at the presynaptic terminal, due (respectively) to two closely paired pulses or to high frequency stimulation, both of which augment neurotransmitter release. PPF and PTP are governed by different synaptic vesicle proteins: e.g., the absence of the synaptic vesicle protein synaptogyrin I in mice causes respectively impaired PTP but no effect on PPF (*74*).

Dutch mice showed altered presynaptic plasticity mechanisms related to the RRP of neurotransmitters. Dutch mice exhibited respectively faster rates of decay and recovery during high frequency stimulation that causes fatigue at the synapses and after synaptic depression. The depletion and replenishment of the RRP of neurotransmitters appear more profound in Dutch mice. The RRP of neurotransmitters refers to a small subset of neurotransmitter-containing vesicles residing close to the presynaptic terminal (either docked or non-docked) and disposed for immediate released during stimulation. Several parameters can affect the decay of the RRP; e.g., replenishment of the RRP could be mediated by the Ca^{2+}-mediated recruitment of vesicles from the reserve pool to the RRP.

The required interplay between pre- and postsynaptic neurons during synaptic plasticity suggests that presynaptic changes could affect activation of postsynaptic neurons eventually leading to long-term synaptic impairments. High frequency stimulation resulted in normal LTP, suggesting that Dutch mice do not display derangement of postsynaptic mechanisms at the ages studied, an observation that could be attributed to compensatory mechanisms. In one possibility, the decrease in release probability with PTP may be balanced by the increased depletion and replenishment of the RRP.

Hippocampal microglia (Cluster 2) did not show a high number of DEGs, nor were differences in expression of microglia DAM and homeostatic signatures observed between Dutch and wildtype mice. The highest total and unique number of DEGs were found in excitatory neurons (Cluster 6) and were associated with processes such as "protein translation" and "electron transport chain". LR pairs were examined between oligodendrocytes and excitatory neurons, which indicated that *Gabbr2* showed stronger interaction with multiple GABA inhibitory neurotransmitter complex partners in Dutch mice.

Finally, prior studies using bulk RNAseq on the entorhinal cortex and dentate gyrus of wildtype and Dutch mice were re-examined using scRNA-seq, revealing no obvious differences in microglial transcriptional profiles. Moreover, the Dutch mouse hippocampal transcriptome did not present neuroinflammatory and microglial transcriptomic responses which are commonly observed in models with senile plaques and amyloid fibrils (e.g., PSAPP, 5XFAD). Failure to capture such a response may be due to the cell populations selected for profiling. Indeed, previous characterization indicated that microgliosis in other Dutch mice (*75*) was not generalized but was limited to the immediate proximity of Aβ-laden vessels. In this study, no differences were observed in

microgliosis, which is reported to be an NFA-Aβ-induced process that drives activation of complement and synapse elimination (*57*). In a transcriptomic analysis on postmortem brain tissue from humans with HCHWAD, inflammatory genes and pathways were also not prominently represented (*76*). As detected in the Dutch mouse, the main pathways over-represented in the human HCHWAD brains were related to mitochondrial dysfunction (*76*). The principal up-regulated pathways entail interactions of the extracellular matrix and transforming growth factor beta signaling. In a clustering analysis to identify molecular subtypes of AD, gene expression profiles have been gleaned from the Mount Sinai Brain Bank (MSBB-AD) and Religious Orders Study-Memory and Aging Project (ROSMAP) (*77*). The Dutch mouse gene signature significantly correlated with the subtype of "typical" or "Aβ predominant" AD presentation, and was characterized by increased immune activation and inflammation, as well as decreased synaptic signaling and dysregulation in neuronal processes and synaptic signaling (*77*). Taken together, the results minimize the contribution of neuroinflammation in the pathogenesis leading to learning disorder in Dutch mice.

Among the most dysregulated pathways in the Dutch mouse brain was "structural constituent of ribosome", which is associated with the most significant GO term in Cluster 6 "protein translation". Increasing evidence suggests that dysregulation of mRNA translation contributes to the pathogenesis of several neurological diseases, including AD (*78*). Accumulation of Aβ is linked to increased protein synthesis through loss of interactions from key translation regulators, particularly translation repressors (*79*). When the cell-type specific transcriptional responses to NFA-Aβ were examined, altered transcriptional profiles were identified in multiple cell types. In these profiles, overlap with GO term enrichment analysis indicated "amyloid-beta binding" among the shared processes.

The Cluster 6 neuron DEGs downregulated in Dutch compared to wildtype mice were associated with mitochondrial functions, specifically GO terms "electron transport chain" and "oxidative phosphorylation". In concordance, cellular respiration pathways were the most significantly altered pathways identified in the transcriptomic analysis from human patients with HCHWAD (*76*). Moreover, fewer and smaller mitochondria were found at the presynaptic terminals of excitatory neurons in the CA1 of Dutch compared to wildtype mice. Strong evidence linking NFA-Aβ to mitochondrial complex I endpoints has come from the combined use of a genetically encoded fluorescent redox sensor and multiphoton microscopy to image and monitor *in vivo* the mitochondrial redox imbalance in neurons from the APP/PS1 transgenic mouse model of AD (*80*). The deposition of Aβ plaque and particularly soluble NFA-Aβ species were shown to lead to increased mitochondrial oxidative stress levels within neuronal mitochondria (*80*). Mitochondrial redox dysregulation in neurons was prevented by inhibition of mitochondrial calcium influx, which is pathologically exacerbated in Aβ plaque-depositing mice (*80*). Furthermore, mitochondria-targeting antioxidants decreased mitochondrial oxidative stress back to basal levels and reverted Aβ plaque-associated dystrophic neurites in the APP/PS1 mice (*80*). Defective mitochondrial

complex I activity has been detected in living human AD brain (*81*). Altered mitochondrial fission and fusion has been observed in the hippocampus of human AD and in Tg2576 mice and may explain the observations of decreased mitochondrial density and smaller mitochondria in Dutch mice (*68, 82*). Increased mitochondrial fragmentation has been reported in neurons exposed to NFA-Aβ (*83*). Elevated levels of NFA-Aβ impaired transport of mitochondria in dendrites and axons and increased mitochondrial permeability in mice harboring the Osaka mutation of APP (APP^{E693D}) (*84, 85*). Mitochondria-targeting therapy holds promise for treating neurodegenerative disease (*86, 87*). Our finding of reduced density of presynaptic mitochondria in the CA1 of Dutch mice suggests that NFA-Aβ might also affect transport of mitochondria to axon terminals. The dysfunction of mitochondria and endoplasmic reticulum (ER) protein translation observed in Dutch mice is consistent with observations in other mouse models of AD (*88*).

In conclusion, two independent methods visualized for the first time *endogenously generated* NFA-Aβ *in vivo* in the absence of intracerebral injection of synthetic peptides and without the concurrent presence of Aβ fibrils. Changes related to the APP^{E693Q}-genotype were revealed in NFA-Aβ histopathology, in expression of mitochondrial and neuronal translation-related genes, in presynaptic physiology, and in the ultrastructure of presynaptic mitochondria. Neuroinflammation is not a major contributor to the pathogenesis in Dutch mice. Neither fibrillar Aβ nor neuroinflammation is required for the aging-related learning behavior phenotype.

This study of APP^{E693Q} mice is particularly timely considering the promising outcome of clinical trials for lecanemab (*89, 90*) and donanemab (*91*). After 18 months of treatment with antibody, participants experiencing mild cognitive impairment due to AD showed respectively a modest but statistically significant 27% and 35% slower rate of cognitive decline with lecanemab and donanemab. The modest clinical response to therapeutic infusion of anti-amyloid antibodies may be attributable, at least in part, to the persistence of residual toxic NFA-Aβ that goes undetected by current fluid biomarker analysis and amyloid fibril imaging. The potential clinical importance of NFA-Aβ is reinforced by the recent discovery of a new FAD mutation (APP^{D678N}) that also favors NFA-Aβ accumulation (*92*). Therapeutic depletion of NFA-Aβ may be required for optimum and more robust cognitive benefits from anti-amyloid antibody infusion. Newer methods for imaging NFA-Aβ (e.g., [^{64}Cu]-NOTA cyclic D,L-α-peptides) in the living human brain (*22*) and assays for detection of NFA-Aβ in biofluids (*93-95*) may provide earlier diagnosis and improved monitoring of patients undergoing Aβ immunodepletion therapy by assuring that both fibrillar and nonfibrillar Aβ conformers are cleared as completely as possible.

References

1. S. W. Scheff, D. A. Price, F. A. Schmitt, S. T. DeKosky, E. J. Mufson, Synaptic alterations in CA1 in mild Alzheimer disease and mild cognitive impairment. *Neurology* 68, 1501-1508 (2007).

2. T. Arendt, Synaptic degeneration in Alzheimer's disease. *Acta Neuropathol* 118, 167-179 (2009).

3. G. M. Shankar, D. M. Walsh, Alzheimer's disease: synaptic dysfunction and Abeta. *Mol Neurodegener* 4, 48 (2009).

4. A. John, P. H. Reddy, Synaptic basis of Alzheimer's disease: Focus on synaptic amyloid beta, P-tau and mitochondria. *Ageing Res Rev* 65, 101208 (2021).

5. M. Pang, L. Zhu, A. Gabelle, A. R. Gafson, R. W. Platt, J. E. Galvin, P. Krolak-Salmon, I. Rubino, C. de Moor, S. Belachew, C. Shen, Effect of reduction in brain amyloid levels on change in cognitive and functional decline in randomized clinical trials: An instrumental variable meta-analysis. *Alzheimers Dement*, (2022).

6. T. Bussière, P. D. Friend, N. Sadeghi, B. Wicinski, G. I. Lin, C. Bouras, P. Giannakopoulos, N. K. Robakis, J. H. Morrison, D. P. Perl, P. R. Hof, Stereologic assessment of the total cortical volume occupied by amyloid deposits and its relationship with cognitive status in aging and Alzheimer's disease. *Neuroscience* 112, 75-91 (2002).

7. A. Akram, D. Christoffel, A. B. Rocher, C. Bouras, E. Kövari, D. P. Perl, J. H. Morrison, F. R. Herrmann, V. Haroutunian, P. Giannakopoulos, P. R. Hof, Stereologic estimates of total spinophilin-immunoreactive spine number in area 9 and the CA1 field: relationship with the progression of Alzheimer's disease. *Neurobiol Aging* 29, 1296-1307 (2008).

8. P. T. Nelson, I. Alafuzoff, E. H. Bigio, C. Bouras, H. Braak, N. J. Cairns, R. J. Castellani, B. J. Crain, P. Davies, K. Del Tredici, C. Duyckaerts, M. P. Frosch, V. Haroutunian, P. R. Hof, C. M. Hulette, B. T. Hyman, T. Iwatsubo, K. A. Jellinger, G. A. Jicha, E. Kövari, W. A. Kukull, J. B. Leverenz, S. Love, I. R. Mackenzie, D. M. Mann, E. Masliah, A. C. McKee, T. J. Montine, J. C. Morris, J. A. Schneider, J. A. Sonnen, D. R. Thal, J. Q. Trojanowski, J. C. Troncoso, T. Wisniewski, R. L. Woltjer, T. G. Beach, Correlation of Alzheimer disease neuropathologic changes with cognitive status: a review of the literature. *J Neuropathol Exp Neurol* 71, 362-381 (2012).

9. K. Ishibashi, T. Tomiyama, K. Nishitsuji, M. Hara, H. Mori, Absence of synaptophysin near cortical neurons containing oligomer Abeta in Alzheimer's disease brain. *J Neurosci Res* 84, 632-636 (2006).

04 10. M. P. Lambert, A. K. Barlow, B. A. Chromy, C. Edwards, R. Freed, M. Liosatos, T. E. Morgan, I. Rozovsky,
05 B. Trommer, K. L. Viola, P. Wals, C. Zhang, C. E. Finch, G. A. Krafft, W. L. Klein, Diffusible, nonfibrillar
06 ligands derived from Abeta1-42 are potent central nervous system neurotoxins. *Proc Natl Acad Sci U S A* 95,
07 6448-6453 (1998).

08 11. J. A. Fein, S. Sokolow, C. A. Miller, H. V. Vinters, F. Yang, G. M. Cole, K. H. Gylys, Co-localization of
09 amyloid beta and tau pathology in Alzheimer's disease synaptosomes. *Am J Pathol* 172, 1683-1692 (2008).

10 12. S. Sokolow, K. M. Henkins, T. Bilousova, C. A. Miller, H. V. Vinters, W. Poon, G. M. Cole, K. H. Gylys,
11 AD synapses contain abundant Aβ monomer and multiple soluble oligomers, including a 56-kDa assembly.
12 *Neurobiol Aging* 33, 1545-1555 (2012).

13 13. T. Bilousova, C. A. Miller, W. W. Poon, H. V. Vinters, M. Corrada, C. Kawas, E. Y. Hayden, D. B. Teplow,
14 C. Glabe, R. Albay, 3rd, G. M. Cole, E. Teng, K. H. Gylys, Synaptic Amyloid-β Oligomers Precede p-Tau and
15 Differentiate High Pathology Control Cases. *Am J Pathol* 186, 185-198 (2016).

16 14. D. M. Walsh, I. Klyubin, J. V. Fadeeva, W. K. Cullen, R. Anwyl, M. S. Wolfe, M. J. Rowan, D. J. Selkoe,
17 Naturally secreted oligomers of amyloid beta protein potently inhibit hippocampal long-term potentiation in
18 vivo. *Nature* 416, 535-539 (2002).

19 15. G. M. Shankar, B. L. Bloodgood, M. Townsend, D. M. Walsh, D. J. Selkoe, B. L. Sabatini, Natural
20 oligomers of the Alzheimer amyloid-beta protein induce reversible synapse loss by modulating an NMDA-type
21 glutamate receptor-dependent signaling pathway. *J Neurosci* 27, 2866-2875 (2007).

22 16. J. P. Cleary, D. M. Walsh, J. J. Hofmeister, G. M. Shankar, M. A. Kuskowski, D. J. Selkoe, K. H. Ashe,
23 Natural oligomers of the amyloid-beta protein specifically disrupt cognitive function. *Nat Neurosci* 8, 79-84
24 (2005).

25 17. B. DaRocha-Souto, T. C. Scotton, M. Coma, A. Serrano-Pozo, T. Hashimoto, L. Serenó, M. Rodríguez, B.
26 Sánchez, B. T. Hyman, T. Gómez-Isla, Brain oligomeric β-amyloid but not total amyloid plaque burden
27 correlates with neuronal loss and astrocyte inflammatory response in amyloid precursor protein/tau transgenic
28 mice. *J Neuropathol Exp Neurol* 70, 360-376 (2011).

29 18. S. Gandy, A. J. Simon, J. W. Steele, A. L. Lublin, J. J. Lah, L. C. Walker, A. I. Levey, G. A. Krafft, E. Levy,
30 F. Checler, C. Glabe, W. B. Bilker, T. Abel, J. Schmeidler, M. E. Ehrlich, Days to criterion as an indicator of
31 toxicity associated with human Alzheimer amyloid-beta oligomers. *Ann Neurol* 68, 220-230 (2010).

19. E. Levy, M. D. Carman, I. J. Fernandez-Madrid, M. D. Power, I. Lieberburg, S. G. van Duinen, G. T. Bots, W. Luyendijk, B. Frangione, Mutation of the Alzheimer's disease amyloid gene in hereditary cerebral hemorrhage, Dutch type. *Science* 248, 1124-1126 (1990).

20. M. L. Maat-Schieman, S. G. van Duinen, J. Haan, R. A. Roos, Morphology of cerebral plaque-like lesions in hereditary cerebral hemorrhage with amyloidosis (Dutch). *Acta Neuropathol* 84, 674-679 (1992).

21. E. M. Knight, S. H. Kim, J. C. Kottwitz, A. Hatami, R. Albay, A. Suzuki, A. Lublin, C. M. Alberini, W. L. Klein, P. Szabo, N. R. Relkin, M. Ehrlich, C. G. Glabe, S. Gandy, J. W. Steele, Effective anti-Alzheimer Abeta therapy involves depletion of specific Abeta oligomer subtypes. *Neurol Neuroimmunol Neuroinflamm* 3, e237 (2016).

22. M. Habashi, S. Vutla, K. Tripathi, S. Senapati, P. S. Chauhan, A. Haviv-Chesner, M. Richman, S.-A. Mohand, V. Dumulon-Perreault, R. Mulamreddy, E. Okun, J. H. Chill, B. Guérin, W. D. Lubell, S. Rahimipour, Early diagnosis and treatment of Alzheimer's disease by targeting toxic soluble Aβ oligomers. *Proceedings of the National Academy of Sciences* 119, e2210766119 (2022).

23. G. Kaur, M. Pawlik, S. E. Gandy, M. E. Ehrlich, J. F. Smiley, E. Levy, Lysosomal dysfunction in the brain of a mouse model with intraneuronal accumulation of carboxyl terminal fragments of the amyloid precursor protein. *Mol Psychiatry* 22, 981-989 (2017).

24. K. A. Price, M. Varghese, A. Sowa, F. Yuk, H. Brautigam, M. E. Ehrlich, D. L. Dickstein, Altered synaptic structure in the hippocampus in a mouse model of Alzheimer's disease with soluble amyloid-beta oligomers and no plaque pathology. *Mol Neurodegener* 9, 41 (2014).

25. B. Readhead, J. V. Haure-Mirande, B. Zhang, V. Haroutunian, S. Gandy, E. E. Schadt, J. T. Dudley, M. E. Ehrlich, Molecular systems evaluation of oligomerogenic APP(E693Q) and fibrillogenic APP(KM670/671NL)/PSEN1(Deltaexon9) mouse models identifies shared features with human Alzheimer's brain molecular pathology. *Mol Psychiatry* 21, 1153-1154 (2016).

26. R. Kayed, E. Head, J. L. Thompson, T. M. McIntire, S. C. Milton, C. W. Cotman, C. G. Glabe, Common structure of soluble amyloid oligomers implies common mechanism of pathogenesis. *Science* 300, 486-489 (2003).

27. C. A. Schneider, W. S. Rasband, K. W. Eliceiri, NIH Image to ImageJ: 25 years of image analysis. *Nat Methods* 9, 671-675 (2012).

60 28. M. Pagnon de la Vega, V. Giedraitis, W. Michno, L. Kilander, G. Güner, M. Zielinski, M. Löwenmark, R.
61 Brundin, T. Danfors, L. Söderberg, I. Alafuzoff, L. N. G. Nilsson, A. Erlandsson, D. Willbold, S. A. Müller, G.
62 F. Schröder, J. Hanrieder, S. F. Lichtenthaler, L. Lannfelt, D. Sehlin, M. Ingelsson, The Uppsala APP deletion
63 causes early onset autosomal dominant Alzheimer's disease by altering APP processing and increasing amyloid
64 β fibril formation. *Sci Transl Med* 13, (2021).

65 29. S. R. Meier, D. Sehlin, G. Hultqvist, S. Syvänen, Pinpointing Brain TREM2 Levels in Two Mouse Models
66 of Alzheimer's Disease. *Mol Imaging Biol* 23, 665-675 (2021).

67 30. J. W. Steele, H. Brautigam, J. A. Short, A. Sowa, M. Shi, A. Yadav, C. M. Weaver, D. Westaway, P. E.
68 Fraser, P. H. St George-Hyslop, S. Gandy, P. R. Hof, D. L. Dickstein, Early fear memory defects are associated
69 with altered synaptic plasticity and molecular architecture in the TgCRND8 Alzheimer's disease mouse model. *J*
70 *Comp Neurol* 522, 2319-2335 (2014).

71 31. M. J. Lazarczyk, J. E. Kemmler, B. A. Eyford, J. A. Short, M. Varghese, A. Sowa, D. R. Dickstein, F. J. Yuk,
72 R. Puri, K. E. Biron, M. Leist, W. A. Jefferies, D. L. Dickstein, Major Histocompatibility Complex class I
73 proteins are critical for maintaining neuronal structural complexity in the aging brain. *Sci Rep* 6, 26199 (2016).

74 32. Y. Hara, M. Punsoni, F. Yuk, C. S. Park, W. G. Janssen, P. R. Rapp, J. H. Morrison, Synaptic distributions of
75 GluA2 and PKMζ in the monkey dentate gyrus and their relationships with aging and memory. *J Neurosci* 32,
76 7336-7344 (2012).

77 33. Y. Hara, C. S. Park, W. G. Janssen, M. T. Roberts, J. H. Morrison, P. R. Rapp, Synaptic correlates of memory
78 and menopause in the hippocampal dentate gyrus in rhesus monkeys. *Neurobiol Aging* 33, 421.e417-428 (2012).

79 34. Y. Han, P. S. Kaeser, T. C. Südhof, R. Schneggenburger, RIM determines Ca^{2+} channel density and vesicle
80 docking at the presynaptic active zone. *Neuron* 69, 304-316 (2011).

81 35. C. Tan, S. S. H. Wang, G. de Nola, P. S. Kaeser, Rebuilding essential active zone functions within a synapse.
82 *Neuron* 110, 1498-1515.e1498 (2022).

83 36. P. G. Camoletto, H. Vara, L. Morando, E. Connell, F. P. Marletto, M. Giustetto, M. Sassoè-Pognetto, P. P.
84 Van Veldhoven, M. D. Ledesma, Synaptic vesicle docking: sphingosine regulates syntaxin1 interaction with
85 Munc18. *PLoS One* 4, e5310 (2009).

86 37. A. Butler, P. Hoffman, P. Smibert, E. Papalexi, R. Satija, Integrating single-cell transcriptomic data across
87 different conditions, technologies, and species. *Nature Biotechnology* 36, 411-420 (2018).

88 38. L. McInnes, J. Healy, UMAP: Uniform Manifold Approximation and Projection for Dimension Reduction.
89 (2018).

90 39. O. Franzén, L. M. Gan, J. L. M. Björkegren, PanglaoDB: a web server for exploration of mouse and human
91 single-cell RNA sequencing data. *Database (Oxford)* 2019, (2019).

92 40. R. Satija, J. A. Farrell, D. Gennert, A. F. Schier, A. Regev, Spatial reconstruction of single-cell gene
93 expression data. *Nat Biotechnol* 33, 495-502 (2015).

94 41. C. Neftel, J. Laffy, M. G. Filbin, T. Hara, M. E. Shore, G. J. Rahme, A. R. Richman, D. Silverbush, M. L.
95 Shaw, C. M. Hebert, J. Dewitt, S. Gritsch, E. M. Perez, L. N. Gonzalez Castro, X. Lan, N. Druck, C. Rodman,
96 D. Dionne, A. Kaplan, M. S. Bertalan, J. Small, K. Pelton, S. Becker, D. Bonal, Q. D. Nguyen, R. L. Servis, J.
97 M. Fung, R. Mylvaganam, L. Mayr, J. Gojo, C. Haberler, R. Geyeregger, T. Czech, I. Slavc, B. V. Nahed, W. T.
98 Curry, B. S. Carter, H. Wakimoto, P. K. Brastianos, T. T. Batchelor, A. Stemmer-Rachamimov, M. Martinez-
99 Lage, M. P. Frosch, I. Stamenkovic, N. Riggi, E. Rheinbay, M. Monje, O. Rozenblatt-Rosen, D. P. Cahill, A. P.
00 Patel, T. Hunter, I. M. Verma, K. L. Ligon, D. N. Louis, A. Regev, B. E. Bernstein, I. Tirosh, M. L. Suvà, An
01 Integrative Model of Cellular States, Plasticity, and Genetics for Glioblastoma. *Cell* 178, 835-849.e821 (2019).

02 42. Y. Chen, M. Colonna, Microglia in Alzheimer's disease at single-cell level. Are there common patterns in
03 humans and mice? *J Exp Med* 218, (2021).

04 43. Y. Hara, F. Yuk, R. Puri, W. G. Janssen, P. R. Rapp, J. H. Morrison, Presynaptic mitochondrial morphology
05 in monkey prefrontal cortex correlates with working memory and is improved with estrogen treatment. *Proc*
06 *Natl Acad Sci U S A* 111, 486-491 (2014).

07 44. S. Tucker, C. Möller, K. Tegerstedt, A. Lord, H. Laudon, J. Sjödahl, L. Söderberg, E. Spens, C. Sahlin, E. R.
08 Waara, A. Satlin, P. Gellerfors, G. Osswald, L. Lannfelt, The murine version of BAN2401 (mAb158) selectively
09 reduces amyloid-β protofibrils in brain and cerebrospinal fluid of tg-ArcSwe mice. *J Alzheimers Dis* 43, 575-
10 588 (2015).

11 45. M. Richman, S. Wilk, M. Chemerovski, S. K. Wärmländer, A. Wahlström, A. Gräslund, S. Rahimipour, In
12 vitro and mechanistic studies of an antiamyloidogenic self-assembled cyclic D,L-α-peptide architecture. *J Am*
13 *Chem Soc* 135, 3474-3484 (2013).

14 46. M. Chemerovski-Glikman, M. Richman, S. Rahimipour, Structure-based study of antiamyloidogenic cyclic
15 d,l-α-peptides. *Tetrahedron* 70, 7639-7644 (2014).

16 47. M. Chemerovski-Glikman, E. Rozentur-Shkop, M. Richman, A. Grupi, A. Getler, H. Y. Cohen, H. Shaked,
17 C. Wallin, S. K. Wärmländer, E. Haas, A. Gräslund, J. H. Chill, S. Rahimipour, Self-Assembled Cyclic d,l-α-
18 Peptides as Generic Conformational Inhibitors of the α-Synuclein Aggregation and Toxicity: In Vitro and
19 Mechanistic Studies. *Chemistry* 22, 14236-14246 (2016).

20 48. A. Belostozky, M. Richman, E. Lisniansky, A. Tovchygrechko, J. H. Chill, S. Rahimipour, Inhibition of tau-
21 derived hexapeptide aggregation and toxicity by a self-assembled cyclic d,l-α-peptide conformational inhibitor.
22 *Chemical Communications* 54, 5980-5983 (2018).

23 49. K. Ono, M. M. Condron, D. B. Teplow, Structure-neurotoxicity relationships of amyloid beta-protein
24 oligomers. *Proc Natl Acad Sci U S A* 106, 14745-14750 (2009).

25 50. R. S. Zucker, W. G. Regehr, Short-term synaptic plasticity. *Annu Rev Physiol* 64, 355-405 (2002).

26 51. H. Zhang, B. Gong, S. Liu, M. Fa, I. Ninan, A. Staniszewski, O. Arancio, Synaptic fatigue is more
27 pronounced in the APP/PS1 transgenic mouse model of Alzheimer's disease. *Curr Alzheimer Res* 2, 137-140
28 (2005).

29 52. G. Yu, L.-G. Wang, Y. Han, Q.-Y. He, clusterProfiler: an R Package for Comparing Biological Themes
30 Among Gene Clusters. *OMICS: A Journal of Integrative Biology* 16, 284-287 (2012).

31 53. M. Ximerakis, S. L. Lipnick, B. T. Innes, S. K. Simmons, X. Adiconis, D. Dionne, B. A. Mayweather, L.
32 Nguyen, Z. Niziolek, C. Ozek, V. L. Butty, R. Isserlin, S. M. Buchanan, S. S. Levine, A. Regev, G. D. Bader, J.
33 Z. Levin, L. L. Rubin, Single-cell transcriptomic profiling of the aging mouse brain. *Nature Neuroscience* 22,
34 1696-1708 (2019).

35 54. S. Krasemann, C. Madore, R. Cialic, C. Baufeld, N. Calcagno, R. El Fatimy, L. Beckers, E. O'Loughlin, Y.
36 Xu, Z. Fanek, D. J. Greco, S. T. Smith, G. Tweet, Z. Humulock, T. Zrzavy, P. Conde-Sanroman, M. Gacias, Z.
37 Weng, H. Chen, E. Tjon, F. Mazaheri, K. Hartmann, A. Madi, J. D. Ulrich, M. Glatzel, A. Worthmann, J.
38 Heeren, B. Budnik, C. Lemere, T. Ikezu, F. L. Heppner, V. Litvak, D. M. Holtzman, H. Lassmann, H. L. Weiner,
39 J. Ochando, C. Haass, O. Butovsky, The TREM2-APOE Pathway Drives the Transcriptional Phenotype of
40 Dysfunctional Microglia in Neurodegenerative Diseases. *Immunity* 47, 566-581.e569 (2017).

41 55. G. D. Manocha, A. M. Floden, K. Rausch, J. A. Kulas, B. A. McGregor, L. Rojanathammanee, K. R. Puig,
42 K. L. Puig, S. Karki, M. R. Nichols, D. C. Darland, J. E. Porter, C. K. Combs, APP Regulates Microglial
43 Phenotype in a Mouse Model of Alzheimer's Disease. *J Neurosci* 36, 8471-8486 (2016).

44 56. H. Keren-Shaul, A. Spinrad, A. Weiner, O. Matcovitch-Natan, R. Dvir-Szternfeld, T. K. Ulland, E. David, K.
45 Baruch, D. Lara-Astaiso, B. Toth, S. Itzkovitz, M. Colonna, M. Schwartz, I. Amit, A Unique Microglia Type
46 Associated with Restricting Development of Alzheimer's Disease. *Cell* 169, 1276-1290.e1217 (2017).

47 57. S. Hong, V. F. Beja-Glasser, B. M. Nfonoyim, A. Frouin, S. Li, S. Ramakrishnan, K. M. Merry, Q. Shi, A.
48 Rosenthal, B. A. Barres, C. A. Lemere, D. J. Selkoe, B. Stevens, Complement and microglia mediate early
49 synapse loss in Alzheimer mouse models. *Science* 352, 712-716 (2016).

50 58. P. Sunderaraman, S. Cosentino, N. Schupf, J. Manly, Y. Gu, S. Barral, MEF2C Common Genetic Variation
51 Is Associated With Different Aspects of Cognition in Non-Hispanic White and Caribbean Hispanic Non-
52 demented Older Adults. *Front Genet* 12, 642327 (2021).

53 59. J. C. Lambert, C. A. Ibrahim-Verbaas, D. Harold, A. C. Naj, R. Sims, C. Bellenguez, A. L. DeStafano, J.
54 C. Bis, G. W. Beecham, B. Grenier-Boley, G. Russo, T. A. Thorton-Wells, N. Jones, A. V. Smith, V. Chouraki,
55 C. Thomas, M. A. Ikram, D. Zelenika, B. N. Vardarajan, Y. Kamatani, C. F. Lin, A. Gerrish, H. Schmidt, B.
56 Kunkle, M. L. Dunstan, A. Ruiz, M. T. Bihoreau, S. H. Choi, C. Reitz, F. Pasquier, C. Cruchaga, D. Craig, N.
57 Amin, C. Berr, O. L. Lopez, P. L. De Jager, V. Deramecourt, J. A. Johnston, D. Evans, S. Lovestone, L.
58 Letenneur, F. J. Morón, D. C. Rubinsztein, G. Eiriksdottir, K. Sleegers, A. M. Goate, N. Fiévet, M. W.
59 Huentelman, M. Gill, K. Brown, M. I. Kamboh, L. Keller, P. Barberger-Gateau, B. McGuiness, E. B. Larson, R.
60 Green, A. J. Myers, C. Dufouil, S. Todd, D. Wallon, S. Love, E. Rogaeva, J. Gallacher, P. St George-Hyslop, J.
61 Clarimon, A. Lleo, A. Bayer, D. W. Tsuang, L. Yu, M. Tsolaki, P. Bossù, G. Spalletta, P. Proitsi, J. Collinge, S.
62 Sorbi, F. Sanchez-Garcia, N. C. Fox, J. Hardy, M. C. Deniz Naranjo, P. Bosco, R. Clarke, C. Brayne, D.
63 Galimberti, M. Mancuso, F. Matthews, S. Moebus, P. Mecocci, M. Del Zompo, W. Maier, H. Hampel, A.
64 Pilotto, M. Bullido, F. Panza, P. Caffarra, B. Nacmias, J. R. Gilbert, M. Mayhaus, L. Lannefelt, H. Hakonarson,
65 S. Pichler, M. M. Carrasquillo, M. Ingelsson, D. Beekly, V. Alvarez, F. Zou, O. Valladares, S. G. Younkin, E.
66 Coto, K. L. Hamilton-Nelson, W. Gu, C. Razquin, P. Pastor, I. Mateo, M. J. Owen, K. M. Faber, P. V. Jonsson,
67 O. Combarros, M. C. O'Donovan, L. B. Cantwell, H. Soininen, D. Blacker, S. Mead, T. H. Mosley, Jr., D. A.
68 Bennett, T. B. Harris, L. Fratiglioni, C. Holmes, R. F. de Bruijn, P. Passmore, T. J. Montine, K. Bettens, J. I.
69 Rotter, A. Brice, K. Morgan, T. M. Foroud, W. A. Kukull, D. Hannequin, J. F. Powell, M. A. Nalls, K. Ritchie,
70 K. L. Lunetta, J. S. Kauwe, E. Boerwinkle, M. Riemenschneider, M. Boada, M. Hiltuenen, E. R. Martin, R.
71 Schmidt, D. Rujescu, L. S. Wang, J. F. Dartigues, R. Mayeux, C. Tzourio, A. Hofman, M. M. Nöthen, C. Graff,
72 B. M. Psaty, L. Jones, J. L. Haines, P. A. Holmans, M. Lathrop, M. A. Pericak-Vance, L. J. Launer, L. A. Farrer,
73 C. M. van Duijn, C. Van Broeckhoven, V. Moskvina, S. Seshadri, J. Williams, G. D. Schellenberg, P. Amouyel,
74 Meta-analysis of 74,046 individuals identifies 11 new susceptibility loci for Alzheimer's disease. *Nat Genet* 45,
75 1452-1458 (2013).

76 60. M. Jang, E. Gould, J. Xu, E. J. Kim, J. H. Kim, Oligodendrocytes regulate presynaptic properties and
77 neurotransmission through BDNF signaling in the mouse brainstem. *Elife* 8, (2019).

78 61. C. Habermacher, M. C. Angulo, N. Benamer, Glutamate versus GABA in neuron-oligodendroglia
79 communication. *Glia* 67, 2092-2106 (2019).

80 62. K. Hoshi, H. Ito, E. Abe, T. J. Fuwa, M. Kanno, Y. Murakami, M. Abe, T. Murakami, A. Yoshihara, Y.
81 Ugawa, T. Saito, T. C. Saido, K. Matsumoto, Y. Yamaguchi, K. Furukawa, H. Arai, M. Kanai, M. Miyajima, H.
82 Arai, N. Ogawa, H. Akatsu, Y. Hashizume, H. Tateno, T. Honda, Y. Hashimoto, Transferrin Biosynthesized in
83 the Brain Is a Novel Biomarker for Alzheimer's Disease. *Metabolites* 11, (2021).

84 63. N. Lemon, E. Canepa, M. A. Ilies, S. Fossati, Carbonic Anhydrases as Potential Targets Against
85 Neurovascular Unit Dysfunction in Alzheimer's Disease and Stroke. *Front Aging Neurosci* 13, 772278 (2021).

86 64. X. Wang, B. E. Figueroa, I. G. Stavrovskaya, Y. Zhang, A. C. Sirianni, S. Zhu, A. L. Day, B. S. Kristal, R.
87 M. Friedlander, Methazolamide and melatonin inhibit mitochondrial cytochrome C release and are
88 neuroprotective in experimental models of ischemic injury. *Stroke* 40, 1877-1885 (2009).

89 65. A. Lee, C. Kondapalli, D. M. Virga, T. L. Lewis, Jr., S. Y. Koo, A. Ashok, G. Mairet-Coello, S. Herzig, M.
90 Foretz, B. Viollet, R. Shaw, A. Sproul, F. Polleux, Aβ42 oligomers trigger synaptic loss through CAMKK2-
91 AMPK-dependent effectors coordinating mitochondrial fission and mitophagy. *Nat Commun* 13, 4444 (2022).

92 66. B. A. Györffy, V. Tóth, G. Török, P. Gulyássy, R. Kovács, H. Vadászi, A. Micsonai, M. E. Tóth, M. Sántha,
93 L. Homolya, L. Drahos, G. Juhász, K. A. Kékesi, J. Kardos, Synaptic mitochondrial dysfunction and septin
94 accumulation are linked to complement-mediated synapse loss in an Alzheimer's disease animal model. *Cell*
95 *Mol Life Sci* 77, 5243-5258 (2020).

96 67. A. Norambuena, H. Wallrabe, R. Cao, D. B. Wang, A. Silva, Z. Svindrych, A. Periasamy, S. Hu, R. E. Tanzi,
97 D. Y. Kim, G. S. Bloom, A novel lysosome-to-mitochondria signaling pathway disrupted by amyloid-β
98 oligomers. *The EMBO Journal* 37, e100241 (2018).

99 68. M. J. Calkins, M. Manczak, P. Mao, U. Shirendeb, P. H. Reddy, Impaired mitochondrial biogenesis,
00 defective axonal transport of mitochondria, abnormal mitochondrial dynamics and synaptic degeneration in a
01 mouse model of Alzheimer's disease. *Hum Mol Genet* 20, 4515-4529 (2011).

02 69. J. S. da Silva, Y. Nonose, F. Rohden, P. C. Lukasewicz Ferreira, F. U. Fontella, A. Rocha, A. W. Brochier, R.
03 V. Apel, T. M. de Lima, B. Seminotti, A. U. Amaral, A. Galina, D. O. Souza, Guanosine Neuroprotection of
04 Presynaptic Mitochondrial Calcium Homeostasis in a Mouse Study with Amyloid-beta Oligomers. *Mol*
05 *Neurobiol* 57, 4790-4809 (2020).

06 70. R. J. Rodenburg, Biochemical diagnosis of mitochondrial disorders. *J Inherit Metab Dis* 34, 283-292 (2011).

07 71. T. L. Emmerzaal, R. J. Rodenburg, H. Tanila, V. Verweij, A. J. Kiliaan, T. Kozicz, Age-Dependent Decrease
08 of Mitochondrial Complex II Activity in a Familial Mouse Model for Alzheimer's Disease. *J Alzheimers Dis* 66,
09 75-82 (2018).

10 72. P. Chiozzi, A. C. Sarti, J. M. Sanz, A. L. Giuliani, E. Adinolfi, V. Vultaggio-Poma, S. Falzoni, F. Di Virgilio,
11 Amyloid β-dependent mitochondrial toxicity in mouse microglia requires P2X7 receptor expression and is
12 prevented by nimodipine. *Sci Rep* 9, 6475 (2019).

13 73. I. Klyubin, D. M. Walsh, W. K. Cullen, J. V. Fadeeva, R. Anwyl, D. J. Selkoe, M. J. Rowan, Soluble
14 Arctic amyloid beta protein inhibits hippocampal long-term potentiation in vivo. *Eur J Neurosci* 19, 2839-2846
15 (2004).

16 74. R. Janz, T. C. Südhof, R. E. Hammer, V. Unni, S. A. Siegelbaum, V. Y. J. N. Bolshakov, Essential roles in
17 synaptic plasticity for synaptogyrin I and synaptophysin I. 24, 687-700 (1999).

18 75. M. C. Herzig, D. T. Winkler, P. Burgermeister, M. Pfeifer, E. Kohler, S. D. Schmidt, S. Danner, D.
19 Abramowski, C. Sturchler-Pierrat, K. Burki, S. G. van Duinen, M. L. Maat-Schieman, M. Staufenbiel, P. M.
20 Mathews, M. Jucker, Abeta is targeted to the vasculature in a mouse model of hereditary cerebral hemorrhage
21 with amyloidosis. *Nat Neurosci* 7, 954-960 (2004).

22 76. L. Grand Moursel, W. M. C. van Roon-Mom, S. M. Kiełbasa, H. Mei, H. P. J. Buermans, L. M. van der
23 Graaf, K. M. Hettne, E. J. de Meijer, S. G. van Duinen, J. F. J. Laros, M. A. van Buchem, P. A. C. t Hoen, S. M.
24 van der Maarel, L. van der Weerd, Brain Transcriptomic Analysis of Hereditary Cerebral Hemorrhage With
25 Amyloidosis-Dutch Type. *Front Aging Neurosci* 10, 102 (2018).

26 77. R. A. Neff, M. Wang, S. Vatansever, L. Guo, C. Ming, Q. Wang, E. Wang, E. Horgusluoglu-Moloch, W.-m.
27 Song, A. Li, E. L. Castranio, J. Tcw, L. Ho, A. Goate, V. Fossati, S. Noggle, S. Gandy, M. E. Ehrlich, P. Katsel,
28 E. Schadt, D. Cai, K. J. Brennand, V. Haroutunian, B. Zhang, Molecular subtyping of Alzheimer's disease using
29 RNA sequencing data reveals novel mechanisms and targets. *Science Advances* 7, eabb5398 (2021).

30 78. A. Jishi, X. Qi, H. C. Miranda, Implications of mRNA translation dysregulation for neurological disorders.
31 *Semin Cell Dev Biol* 114, 11-19 (2021).

32 79. A. Ghosh, K. Mizuno, S. S. Tiwari, P. Proitsi, B. Gomez Perez-Nievas, E. Glennon, R. T. Martinez-Nunez,
33 K. P. Giese, Alzheimer's disease-related dysregulation of mRNA translation causes key pathological features
34 with ageing. *Translational Psychiatry* 10, 192 (2020).

35 80. M. Calvo-Rodriguez, S. S. Hou, A. C. Snyder, E. K. Kharitonova, A. N. Russ, S. Das, Z. Fan, A.
36 Muzikansky, M. Garcia-Alloza, A. Serrano-Pozo, E. Hudry, B. J. Bacskai, Increased mitochondrial calcium
37 levels associated with neuronal death in a mouse model of Alzheimer's disease. *Nat Commun* 11, 2146 (2020).

38 81. A. V. Venkataraman, A. Mansur, G. Rizzo, C. Bishop, Y. Lewis, E. Kocagoncu, A. Lingford-Hughes, M.
39 Huiban, J. Passchier, J. B. Rowe, H. Tsukada, D. J. Brooks, L. Martarello, R. A. Comley, L. Chen, A. J.
40 Schwarz, R. Hargreaves, R. N. Gunn, E. A. Rabiner, P. M. Matthews, Widespread cell stress and mitochondrial
41 dysfunction occur in patients with early Alzheimer's disease. *Sci Transl Med* 14, eabk1051 (2022).

42 82. X. Wang, B. Su, H. G. Lee, X. Li, G. Perry, M. A. Smith, X. Zhu, Impaired balance of mitochondrial fission
43 and fusion in Alzheimer's disease. *J Neurosci* 29, 9090-9103 (2009).

44 83. C. D. Sanmartin, T. Adasme, C. Hidalgo, A. C. Paula-Lima, The antioxidant N-acetylcysteine prevents the
45 mitochondrial fragmentation induced by soluble amyloid-beta peptide oligomers. *Neurodegener Dis* 10, 34-37
46 (2012).

47 84. T. Umeda, T. Tomiyama, N. Sakama, S. Tanaka, M. P. Lambert, W. L. Klein, H. Mori, Intraneuronal amyloid
48 beta oligomers cause cell death via endoplasmic reticulum stress, endosomal/lysosomal leakage, and
49 mitochondrial dysfunction in vivo. *J Neurosci Res* 89, 1031-1042 (2011).

50 85. T. Umeda, E. M. Ramser, M. Yamashita, K. Nakajima, H. Mori, M. A. Silverman, T. Tomiyama,
51 Intracellular amyloid β oligomers impair organelle transport and induce dendritic spine loss in primary neurons.
52 *Acta Neuropathol Commun* 3, 51 (2015).

53 86. D. Shea, E. Colasurdo, A. Smith, C. Paschall, S. Jayadev, C. D. Keene, D. Galasko, A. Ko, G. Li, E.
54 Peskind, V. Daggett, SOBA: Development and testing of a soluble oligomer binding assay for detection of
55 amyloidogenic toxic oligomers. *Proc Natl Acad Sci U S A* 119, e2213157119 (2022).

56 87. E. H. Choi, M. H. Kim, S. J. Park, Targeting Mitochondrial Dysfunction and Reactive Oxygen Species for
57 Neurodegenerative Disease Treatment. *Int J Mol Sci* 25, (2024).

58 88. L. Hedskog, C. M. Pinho, R. Filadi, A. Rönnbäck, L. Hertwig, B. Wiehager, P. Larssen, S. Gellhaar, A.
59 Sandebring, M. Westerlund, C. Graff, B. Winblad, D. Galter, H. Behbahani, P. Pizzo, E. Glaser, M. Ankarcrona,
60 Modulation of the endoplasmic reticulum–mitochondria interface in Alzheimer's disease and related models.
61 *Proceedings of the National Academy of Sciences* 110, 7916-7921 (2013).

62 89. C. H. van Dyck, C. J. Swanson, P. Aisen, R. J. Bateman, C. Chen, M. Gee, M. Kanekiyo, D. Li, L.
63 Reyderman, S. Cohen, L. Froelich, S. Katayama, M. Sabbagh, B. Vellas, D. Watson, S. Dhadda, M. Irizarry, L.
64 D. Kramer, T. Iwatsubo, Lecanemab in Early Alzheimer's Disease. *New England Journal of Medicine*, (2022).

65 90. S. Gandy, M. E. Ehrlich, Moving the Needle on Alzheimer's Disease with an Anti-Oligomer Antibody. *N*
66 *Engl J Med* 388, 80-81 (2023).

91. J. R. Sims, J. A. Zimmer, C. D. Evans, M. Lu, P. Ardayfio, J. Sparks, A. M. Wessels, S. Shcherbinin, H. Wang, E. S. Monkul Nery, E. C. Collins, P. Solomon, S. Salloway, L. G. Apostolova, O. Hansson, C. Ritchie, D. A. Brooks, M. Mintun, D. M. Skovronsky, Donanemab in Early Symptomatic Alzheimer Disease: The TRAILBLAZER-ALZ 2 Randomized Clinical Trial. *Jama* 330, 512-527 (2023).

92. H. Sun, Y. Wang, Y. Wang, F. Zeng, Case of Autosomal Dominant Alzheimer Disease With Negative Findings From PiB-PET Examination. *Neurol Genet* 10, e200119 (2024).

93. J. Xu, W. Du, Y. Zhao, K. Lim, L. Lu, C. Zhang, L. Li, Mitochondria targeting drugs for neurodegenerative diseases-Design, mechanism and application. *Acta Pharm Sin B* 12, 2778-2789 (2022).

94. E. Andersson, N. Lindblom, S. Janelidze, G. Salvadó, E. Gkanatsiou, L. Söderberg, C. Möller, L. Lannfelt, J. Ge, J. Hanrieder, K. Blennow, T. Deierborg, N. Mattsson-Carlgren, H. Zetterberg, G. Gouras, O. Hansson, Soluble cerebral Aβ protofibrils link Aβ plaque pathology to changes in CSF Aβ(42)/Aβ(40) ratios, neurofilament light and tau in Alzheimer's disease model mice. *Nat Aging* 5, 366-375 (2025).

95. M. Noguchi-Shinohara, K. Shuta, H. Murakami, Y. Mori, J. Komatsu, C. Kobayashi, S. Hersch, K. Horie, K. Ono, Lecanemab-Associated Amyloid-β Protofibril in Cerebrospinal Fluid Correlates with Biomarkers of Neurodegeneration in Alzheimer's Disease. *Ann Neurol* 97, 993-1006 (2025).

Acknowledgments

We would like to thank all the members of the Dickstein, Arancio, Levy, Rahimipour, Lubell, Guerin, and Ehrlich/Gandy laboratories, and William G. M. Janssen, Allison Sowa, Daniel R. Dickstein, Frank Yuk, and Michael Ragusa for technical assistance and discussion. The authors would like to thank Yanzhuang Wang (Shenzhen Bay Laboratory), and Gary Gibson, Giovanni Manfredi, and Csaba Konrad (all from Weill Cornell Medical College) for valuable conversations and suggestions. We also thank Tamas Kozicz and Graeme Preston (Icahn School of Medicine at Mount Sinai) for performing the electron transport chain activity assays.

Conflicts

Dr. Gandy is a co-founder of Recuerdo Pharmaceuticals. He has served as a consultant in the past for J&J, Diagenic, and Pfizer, and he currently consults for Cognito Therapeutics, GLG Group, SVB Securities, Guidepoint, Third Bridge, MEDACORP, Altpep, Vigil Neurosciences, Memory Garden, and Eisai. He has received research support in the past from Warner-Lambert, Pfizer, Baxter, and Avid. The authors declare no other competing interests.

Funding

National Institutes of Health grant F32AG077900 (ELC)
National Institutes of Health grant P30 AG066514 to Mary Sano with Developmental Pilot Award (ELC, SG)

National Institutes of Health grant U01AG046170 (SG, MEE, MW, BZ)
National Institutes of Health grant RF1AG058469 (SG, MEE)
National Institutes of Health grant RF1AG059319 (SG, MEE)
National Institutes of Health grant R01AG061894 (SG, MEE)
Cure Alzheimer's Fund (SG, MEE, SR, BG, WL)
National Institutes of Health grant RF1AG057440 (MW, BZ)
National Institutes of Health grant RF1AG056507 (CG)
National Institutes of Health grant AG056732 (EL)
National Institutes of Health grant RF1AG086510 (EL)
National Institutes of Health grant R01NS110024 (OA)
Alzheimer's Association NIRG-12-242386 (DLD)
Medical Student Training in Aging Research Program Scientific Fellowship from the American Federation for Aging Research (EB)
The I. M. Ertegun Project for Cognitive Health Extension (SG, MEE)
National Institutes of Health grant RF1AG077828 (MW)
National Institutes of Health grant R21AG077168 (MW)
Alzheimer's Association AARG-22-928419 (MW)
AMED under Grant Number JP24wm0625509 (KA)
Grant-in-Aid for Scientific Research (B) [24K02860] (KA)

Consent was unnecessary. No human subjects were involved in this study.

Author contributions:

Conceptualization: MEE, SG, EL, DLD, OA
Methodology: EB, MV, DLD, KT, SH, JVDL, OA, EA, ELC, CDS, MW, BZ, CG, SR, YH
Investigation: RT, MV, DL, EB, DLD, FG, ELC, KT, SH, JVDL, OA, EA, HZ, BZ, MW, CDS, LS, LL, MI, SR, AA, KA, TS, YH
Visualization: MV, DLD, KT, SH, ELC, MW
Supervision: MEE, SG, EL, DLD, OA
Writing—original draft: MV, DLD, EB, ELC, SG, EA, OA, MW
Writing—review & editing: MV, DLD, ELC, SG, MEE, EL, CG, SR, WL, BG, TS, YH

Data and materials availability

The scRNA-seq data (cell ranger processed count matrices) are in a Synapse repository (accession syn52752404, with direct link https://www.synapse.org/#!Synapse:syn52752404/files/). All data are available in the main text or the supplementary materials." The APP^{E693Q} transgenic mouse can be provided by Thomas Jefferson University pending scientific review and a completed material transfer agreement. Requests for the APP^{E693Q} transgenic mouse should be submitted to michelle.ehrlich@mssm.edu.

Disclaimer

The opinions expressed herein are those of the authors and are not necessarily representative of those of the government of the United States, the Uniformed Services University of the Health Sciences, the Department of Defense (DoD), or the United States Army, Navy or Air Force or the Henry M. Jackson Foundation for the Advancement of Military Medicine, Inc.

Keywords

Proteinopathy; amyloidosis; oligomer; protofibril; synapse; electrophysiology; electron microscopy; transcriptomics

Legends

Figure 1. Aging-related accumulation of NFA-Aβ in the cerebral cortex (a)-(c) and thalamus (d) of APP^{E693Q} transgenic mice revealed by double labeling with A11 epitomic immunohistochemistry and CP-2 cyclic peptide-FITC fluorescence microscopy. Representative images from 2-month-old and 24-month-old Dutch mice showing fluorescence microscopy using DAPI, A11 staining with AlexaFluor-680 secondary antibody (red), and CP-2 cyclic peptideFITC (CP-2-FITC, green)(*22*). Upper right panel is a merge of A11 and CP-2-FITC images. Scale bar = 100 µm. Quantification of A11-immunoreactive and CP-2-FITC-immunoreactive NFA-Aβ aggregates in 2- and 24-mo Dutch shown at bottom right. ** $p < 0.01$.

Figure 2. Dutch mice do not exhibit impairment in basal synaptic transmission or LTP but showed impairment of certain measurements of short-term synaptic plasticity. (A, B) Basal neurotransmission **(A)** and LTP **(B)** are unimpaired in hippocampal slices from Dutch mice as compared to slices from wildtype littermates at the age of 7 to 7.5 months ($F_{(1,28)}$ =0.0026, p=0.959 and $F_{(1,28)}$ =0.219, p=0.644, respectively). **(C-D)** Slices from Dutch mice do not exhibit impairment of basal neurotransmission **(C)** and LTP **(D)** at the age of 10.5 to 11 months compared to wildtype mice ($F_{(1,18)}$ =0.116, p=0.737 and $F_{(1,18)}$ =0.017, =0.899, respectively). **(E)** Dutch mice showed no impairment in paired-pulse facilitation at the age of 11 to 13 months old ($F_{(1, 220)}$ =0.06364, p=0.8011; 2-way ANOVA). **(F)** Post-tetanic potentiation was significantly reduced in slices from 11- to 13-month-old Dutch mice compared to wildtype ($F_{(1,36)}$ =4.771, p=0.036; 2-way ANOVA for the first 6 points after potentiation). **(G)** Significant differences were observed in synaptic fatigue when comparing slices from Dutch mice and wildtype littermates (k=2.247±0.1622 for wildtype and k=2.782±0.1634 for Dutch, p=0.015, k: rate of exponential decay). **(H)** The rate of synaptic vesicle replenishment following a 100 Hz stimulation was found to be significantly increased in hippocampal slices from Dutch mice as compared to slices from wildtype littermates (k=7.509±0.7277 for wildtype, k=13.64±1.682 for Dutch, p<0.0001, k: rate of exponential growth).

68
69 **Figure 3. Distribution and ultrastructure of mGluR-2/3-labeled synapses were comparable in the CA1 of**
70 **12-month-old Dutch and wildtype mice.** mGluR-2/3-labeled synapses were defined as having ≥1 immunogold
71 particle located in the PSD or synaptic cleft. **(A-C)** No significant differences were observed between Dutch and
72 wildtype mice in percentage of mGluR-2/3-labeled total, perforated, and non-perforated synapses, respectively.
73 **(D-F)** Average PSD area of mGluR-2/3labeled synapses for all synapses, non-perforated synapses, and perforated
74 synapses, respectively. Dutch mice had larger PSD area of mGluR-2/3-labeled non-perforated synapses than
75 wildtype (p= 0.04, by unpaired t test), whereas perforated synapses or total synapses were comparable between
76 the two groups. **(G-I)** No significant difference was observed in density of immuno-gold particles in mGluR-2/3-
77 labeled synapses, calculated as number of immuno-gold particles/ PSD area, for all synapses, non-perforated
78 synapses, and perforated synapses, respectively. Data are mean ± SD from n = 5 wildtype, and n = 4 Dutch mice.
79
80 **Figure 4. Transcriptional responses in Dutch mouse brains. (A)** scRNA-seq of hippocampal tissues from 12-
81 month-old male and female Dutch and wildtype mice (n=2 samples per sex per genotype with 3 mice pooled per
82 sample). UMAP plot showing 14 distinguishable clusters (0-13). **(B)** Violin plots illustrating expression of marker
83 genes for each cell type. **(C)** UpSet plot highlighting the overlapping and unique genes between the clusters. **(D)**
84 Bar plot showing number of DEGs per cluster by directionality.
85
86 **Figure 5. Overlapping transcriptomic profiles highlight processes impacted in multiple cell types. (A)** Dot
87 plot highlighting shared GO term enrichment across clusters. **(B-C)** Dot plot of genes associated with shared
88 GO terms **(B) "**structural constituent of ribosome" and **(C) "**amyloid-beta binding", split into Dutch and
89 wildtype mice across all clusters. Wildtype mice are in blue, Dutch mice are in purple. **(D)** UpSet plot
90 comparing overlap of cluster DEGs (adj. p-value <0.05) with previously defined aging gene list. **(E)** Heatmap of
91 log2FC of genes shared with aging gene list.
92
93 **Figure 6. Microglia transcriptomic profiles are similar between Dutch and wildtype mice. (A)** UMAP plot
94 showing sub-clustering analysis results for Cluster 2 microglia, identifying 3 subpopulations of microglia with
95 UMAP plot split by genotype to the right. **(B)** UMAP plots showing expression of previously identified microglial
96 signatures; DAM(*33*), homeostatic, IFN and MHC(*34*). **(C)** Violin plots showing expression across subclusters
97 by genotypes of selected homeostatic microglial genes.
98
99 **Figure 7. Transcriptional profile of Cluster 6 excitatory neurons is altered in Dutch mice. (A)** Volcano plot
00 of genes enriched in Cluster 6 as calculated by pseudobulk differential expression analysis. Red genes are Log2FC

> 0.25 and adj. p-value < 0.05, blue Log2FC < 0.25 and adj. p-value < 0.05, green genes are Log2FC > 0.25 and adj. p-value > 0.05, and grey genes are Log2FC < 0.25 and adj. p-value > 0.05. **(B-C)** GO term analysis of **(B)** upregulated and **(C)** downregulated genes enriched in Cluster 6 (adj. p-value < 0.05) using metascape(*91*). **(D)** Dot plot of DEGs unique to Cluster 6.

Figure 8. Fewer mitochondria were present in presynaptic boutons at excitatory synapses in the CA1 of 12-month-old Dutch mice compared to wildtype. **(A)** Electron micrographs showing representative examples of presynaptic mitochondria (blue masks). **(B)** Curved presynaptic mitochondria demonstrate a bend of at least 90°. Straight presynaptic mitochondria did not exhibit any curvature. Scale bar = 500 nm. **(C)** Total number, **(D)** number of straight mitochondria, **(E)** number of curved mitochondria, **(F)** percentage of curved mitochondria, **(G)** average diameter, and **(H)** number of layers traversed by each mitochondrion in wildtype and Dutch mice. Data are mean ± SD from n = 4 wildtype and n = 5 Dutch mice.

073 **Supplementary Materials Table of Contents**

1074 Supplementary Methods
1075 Figs. S1 to S16
1076 References (92 to 102)

Supplementary Tables Titles and Captions

Supplementary Table 1. Antibodies used in this study.

Supplementary Table 2. Oligomer level and electrophysiological data analyzed by sex.

Supplementary Table 3. Cluster Cell Numbers. Number of cells per cluster per sample.

Supplementary Table 4. Cluster Markers. De novo cluster signatures calculated by comparing cell clusters using Wilcox rank sum test in Seurat.

Supplementary Table 5. Cluster DEGs. Differentially expressed genes across all 14 clusters using MAST implemented in Seurat.

Supplementary Table 6. Cluster 6 GO-terms. GO-term analysis of genes enriched in Cluster 6 (l2f>0, padj <0.05) using metascape.

Supplementary Table 7. Cluster 6 GO-terms. GO-term analysis of genes enriched in Cluster 6 (l2f<0, padj <0.05) using metascape.

Supplementary Table 8. Cluster 4 GO-terms. GO-term analysis of genes enriched in Cluster 6 (l2f>0, padj <0.05) using metascape.

Supplementary Table 9. Ligand-Receptor Pairs for Clusters 6 and 4. Cell-cell communication analysis calculated by Cellphone DB to compute interaction between Clusters 6 and Clusters 9 based on known Ligand-Receptor pairs. t-test was used to compare interaction strength differences between Dutch and WT mice

Supplementary Table 10. Mitochondrial electron transport chain (mETC) enzymology. mETC complexes standardized to μg protein.

Supplementary Table 11. Mitochondrial electron transport chain (mETC) enzymology. mETC complexes standardized to mU/ml citrate synthase.

Highlights

- Transgenic *APP*^{E693Q} mice develop learning behavior changes associated with accumulation of nonfibrillar aggregates of Dutch Aβ in their brains.
- Electrophysiology shows aging-related defects in post-tetanic potentiation, synaptic fatigue, and synaptic vesicle replenishment in *APP*^{E693Q} mice.
- Single cell transcriptomics did not identify the signature of disease-associated microglia, but the significant association of C1q with synaptic puncta indicates activation of the innate immunity pathway leading to microglial engulfment of synapses.
- Ultrastructural analysis showed that Dutch mice have fewer and smaller mitochondria in CA1 presynaptic boutons. Excitatory neurons show changes in endoplasmic reticulum- and mitochondria-related transcripts. Activity of mitochondrial complex I (but not complexes II, III, or IV) is diminished in an aging-related fashion in the *APP*^{E693Q} mouse hippocampus.

RESEARCH IN CONTEXT

1. **Systematic review**: The authors reviewed previous publications using traditional sources, including PubMed and preprint server databases. Nonfibrillar aggregates (NFAs), oligomers, and protofibrils have been frequently studied using synthetic peptides or cell media. There are relatively few peer-reviewed publications regarding endogenously generated nonfibrillar aggregates of Aβ in the brain and/or within the context of Alzheimer's disease (AD). We have cited relevant publications.

2. **Interpretation**: Our results show that aging-related accumulation of NFA-Aβ in APP^{E693Q} mice could be visualized using A11 immunohistochemistry or NFA-Aβ-detecting cyclic D,L-α-peptide-FITC microscopy. The presynaptic termini of APP^{E693Q} mice developed aging-related physiological abnormalities in post-tetanic potentiation, synaptic fatigue, and synaptic vesicle replenishment. Single-cell RNA sequencing showed that excitatory neurons exhibited the most altered transcriptomic profile, especially involving “protein translation” and “oxidative phosphorylation”. Direct measurements of electron transport chain catalysis revealed an aging-related reduction in mitochondrial complex I activity in the hippocampi of Dutch mice. Microglial transcript analysis revealed no evidence of inflammation.

3. **Future directions**: Accumulation of endogenously generated Dutch NFA-Aβ can be visualized with new ligands and alters neuronal metabolism but does not activate inflammation. Since endogenously generated NFA-Aβ is associated with learning behavior changes, the depletion or neutralization of *both fibrillar and NFA-Aβ* may be needed for complete elimination of Aβ toxicity when anti-amyloid antibodies are used clinically.

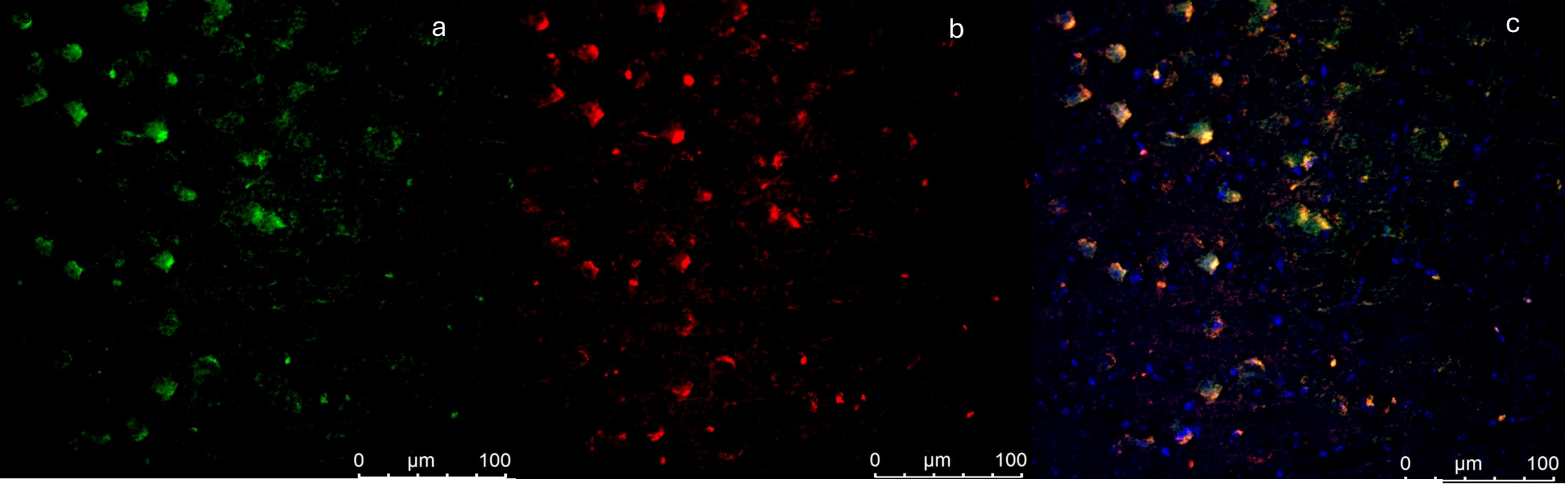
a
b
c
0 µm 100
0 µm 100
0 µm 100

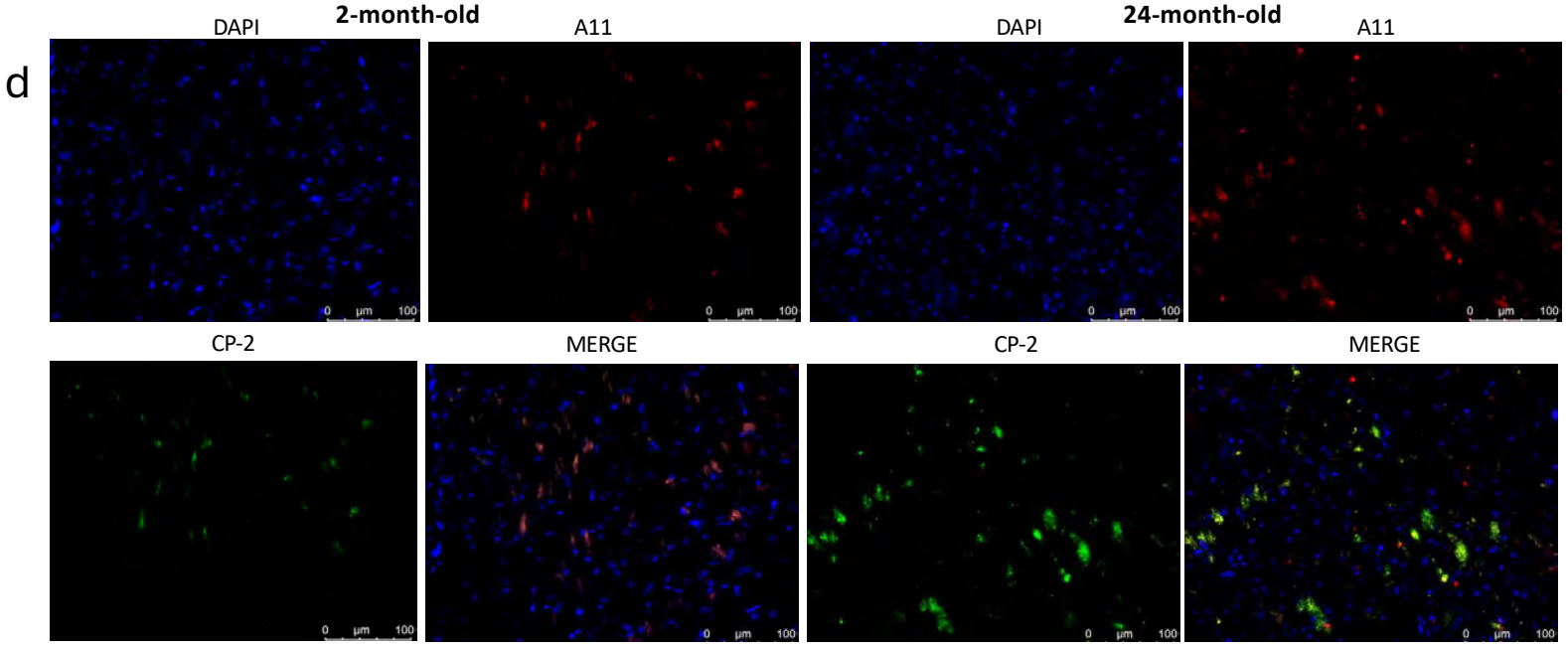
d
2-month-old
24-month-old
DAPI
A11
DAPI
A11
CP-2
MERGE
CP-2
MERGE

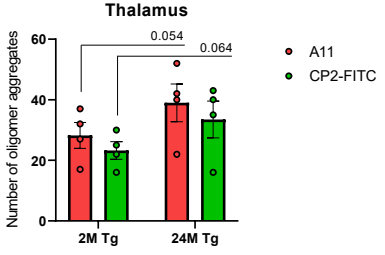
Thalamus
Number of oligomer aggregates
0
20
40
60
0.054
0.064
2M Tg
24M Tg
A11
CP2-FITC

Figure 2

Figure 2. Dutch mice do not exhibit impairment in basal synaptic transmission or LTP but showed impairment of certain measurements of short-term synaptic plasticity. (A, B) Basal neurotransmission **(A)** and LTP **(B)** are unimpaired in hippocampal slices from Dutch mice as compared to slices from wildtype littermates at the age of 7 to 7.5 months ($F_{(1,28)}$ =0.0026, p=0.959 and $F_{(1,28)}$ =0.219, p=0.644, respectively). **(C-D)** Slices from Dutch mice do not exhibit impairment of basal neurotransmission **(C)** and LTP **(D)** at the age of 10.5 to 11 months compared to wildtype mice ($F_{(1,18)}$ =0.116, p=0.737 and $F_{(1,18)}$ =0.017, =0.899, respectively). **(E)** Dutch mice showed no impairment in paired-pulse facilitation at the age of 11 to 13 months old ($F_{(1, 220)}$ =0.06364, p=0.8011; 2-way ANOVA). **(F)** Post-tetanic potentiation was significantly reduced in slices from 11- to 13-month-old Dutch mice compared to wildtype ($F_{(1,36)}$ =4.771, p=0.036; 2-way ANOVA for the first 6 points after potentiation). **(G)** Significant differences were observed in synaptic fatigue when comparing slices from Dutch mice and wildtype littermates (k=2.247±0.1622 for wildtype and k=2.782±0.1634 for Dutch, p=0.015, k: rate of exponential decay). **(H)** The rate of synaptic vesicle replenishment following a 100 Hz stimulation was found to be significantly increased in hippocampal slices from Dutch mice as compared to slices from wildtype littermates (k=7.509±0.7277 for wildtype, k=13.64±1.682 for Dutch, p<0.0001, k: rate of exponential growth). (Wildtype 8 male, 41 female; Dutch 3 male, 44 female).

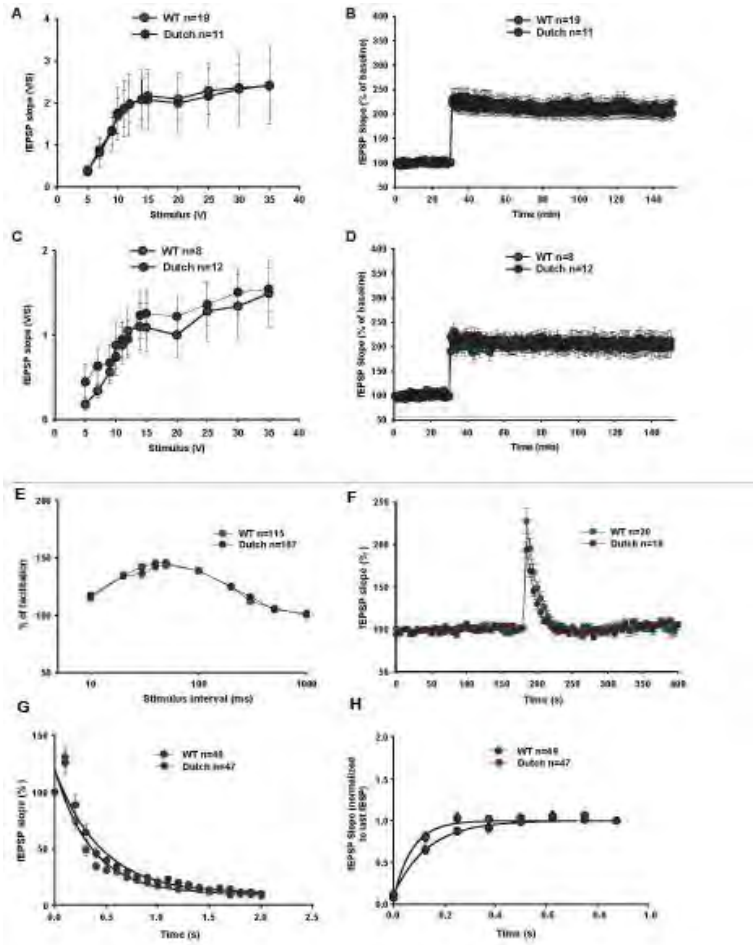

Figure 3

Figure 3. Distribution and ultrastructure of mGluR-2/3-labeled synapses were comparable in the CA1 of 12-month-old Dutch and wildtype mice. mGluR-2/3-labeled synapses were defined as having ≥1 immunogold particle located in the PSD or synaptic cleft. **(A-C)** No significant differences were observed between Dutch and wildtype mice in percentage of mGluR-2/3-labeled total, perforated, and non-perforated synapses, respectively. **(D-F)** Average PSD area of mGluR-2/3labeled synapses for all synapses, non-perforated synapses, and perforated synapses, respectively. Dutch mice had larger PSD area of mGluR-2/3-labeled non-perforated synapses than wildtype ($p= 0.04$, by unpaired t test), whereas perforated synapses or total synapses were comparable between the two groups. **(G-I)** No significant difference was observed in density of immuno-gold particles in mGluR-2/3-labeled synapses, calculated as number of immuno-gold particles/ PSD area, 767 for all synapses, non-perforated synapses, and perforated synapses, respectively. Data are mean ± SD from n = 5 wildtype (2 male and 3 female), and n = 4 (3 male and 1 female) Dutch mice.

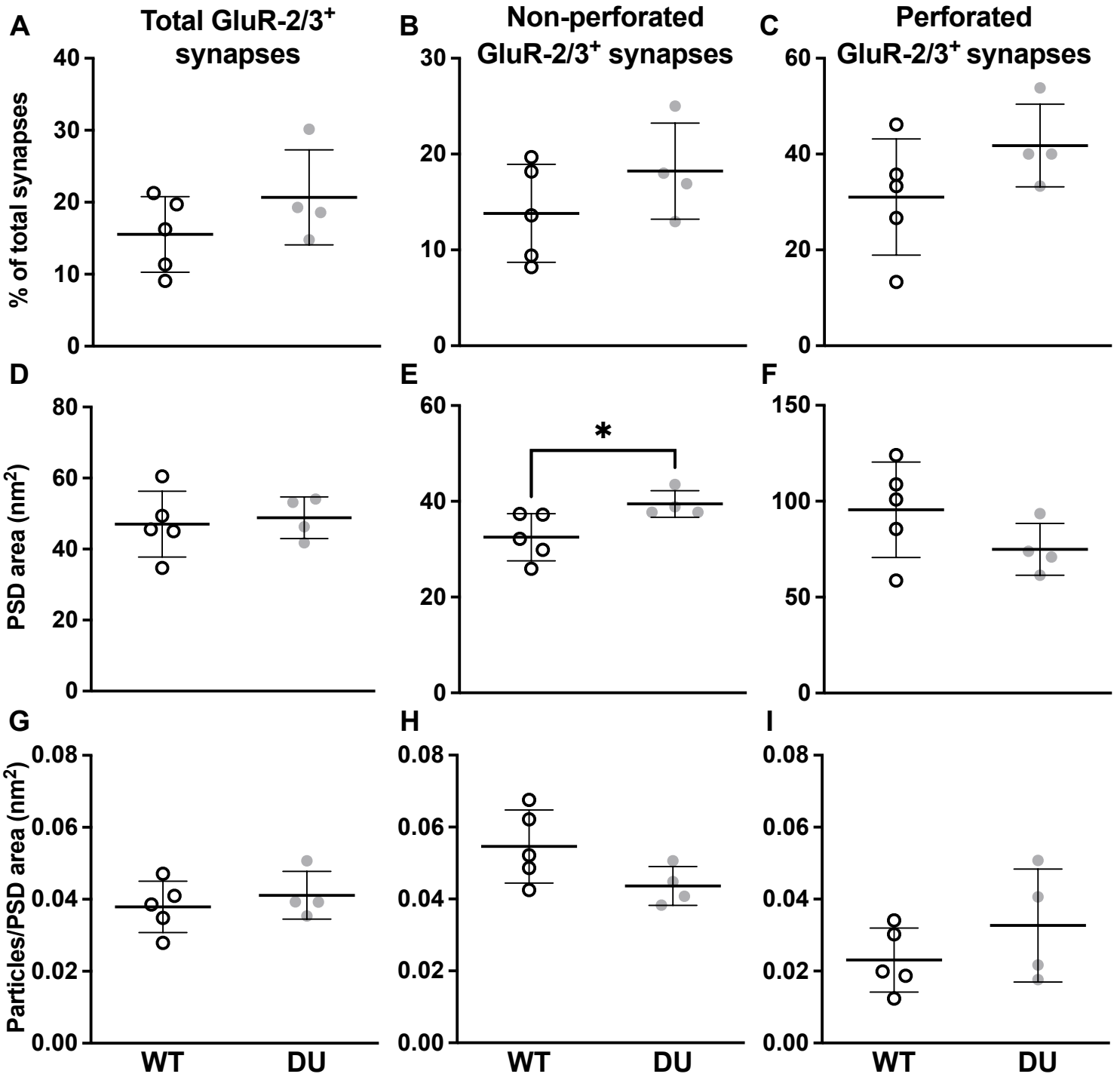
A
Total GluR-2/3+ synapses
B
Non-perforated GluR-2/3+ synapses
C
Perforated GluR-2/3+ synapses
% of total synapses
D
E
F
PSD area (nm2)
*
G
H
I
Particles/PSD area (nm2)
WT
DU
WT
DU
WT
DU

-igure 4

Figure 4. Transcriptional responses in Dutch mouse brains. (A) scRNA-seq of hippocampal tissues from 12-month-old male and female Dutch and wildtype mice (n=2 samples per sex per genotype with 3 mice pooled per sample). UMAP plot showing 14 distinguishable clusters (0-13). **(B)** Violin plots illustrating expression of marker genes for each cell type. **(C)** UpSet plot highlighting the overlapping and unique genes between the clusters. **(D)** Bar plot showing number of DEGs per cluster by directionality. (Wildtype, 1 male and 3 female; Dutch, 3 male and 1 female).

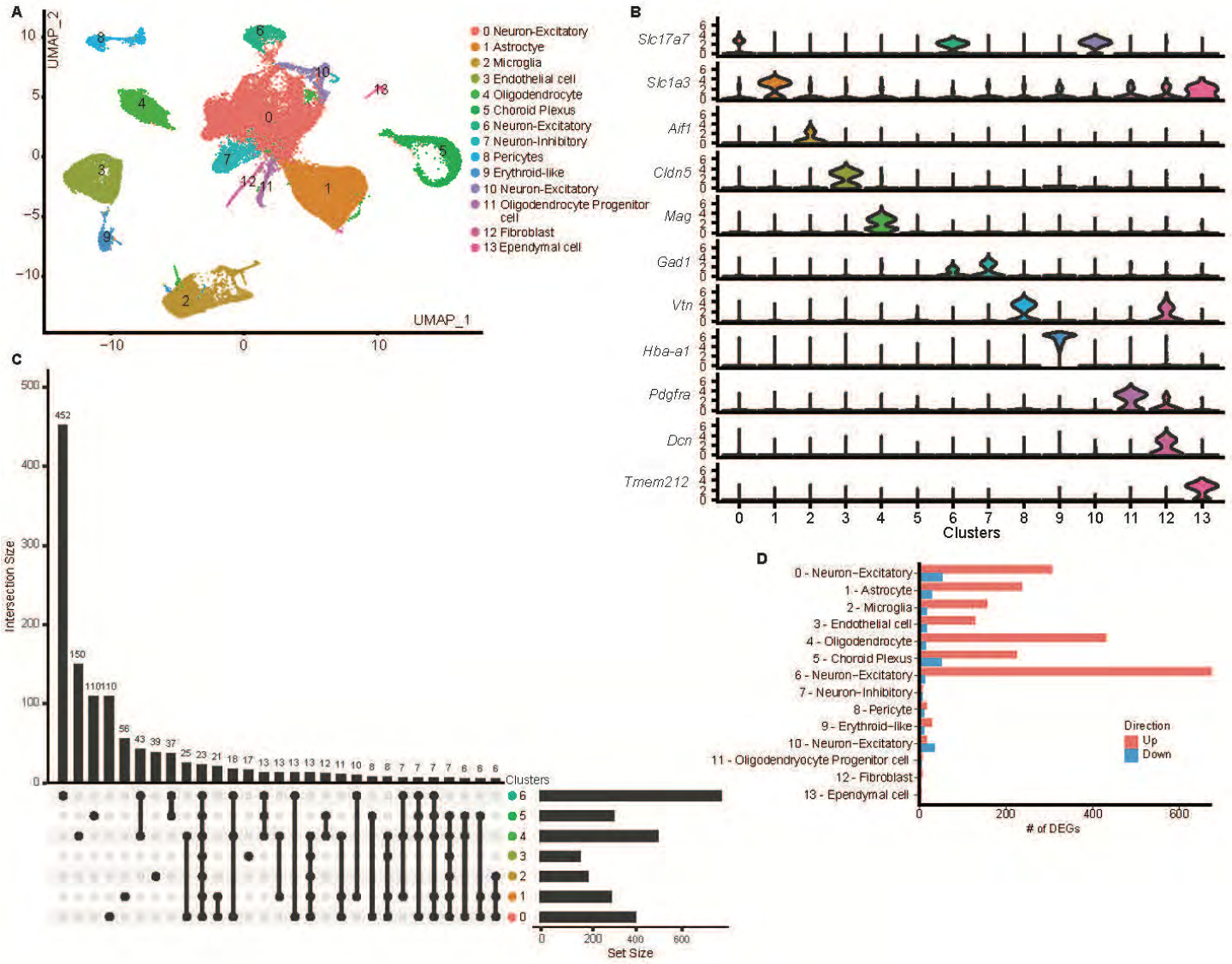

Figure 5

Figure 5. Overlapping transcriptomic profiles highlight processes impacted in multiple cell types. (A) Dot plot highlighting shared GO term enrichment across clusters. **(B-C)** Dot plot of genes associated with shared GO terms **(B) "**structural constituent of ribosome" and **(C)** **“**amyloid-beta binding", split into Dutch and wildtype mice across all clusters. Wildtype mice are in blue, Dutch mice are in purple. **(D)** UpSet plot comparing overlap of cluster DEGs (adj. p-value <0.05) with previously defined aging gene list. **(E)** Heatmap of log2FC of genes shared with aging gene list. (Wildtype, 1 male and 3 female; Dutch, 3 male and 1 female).

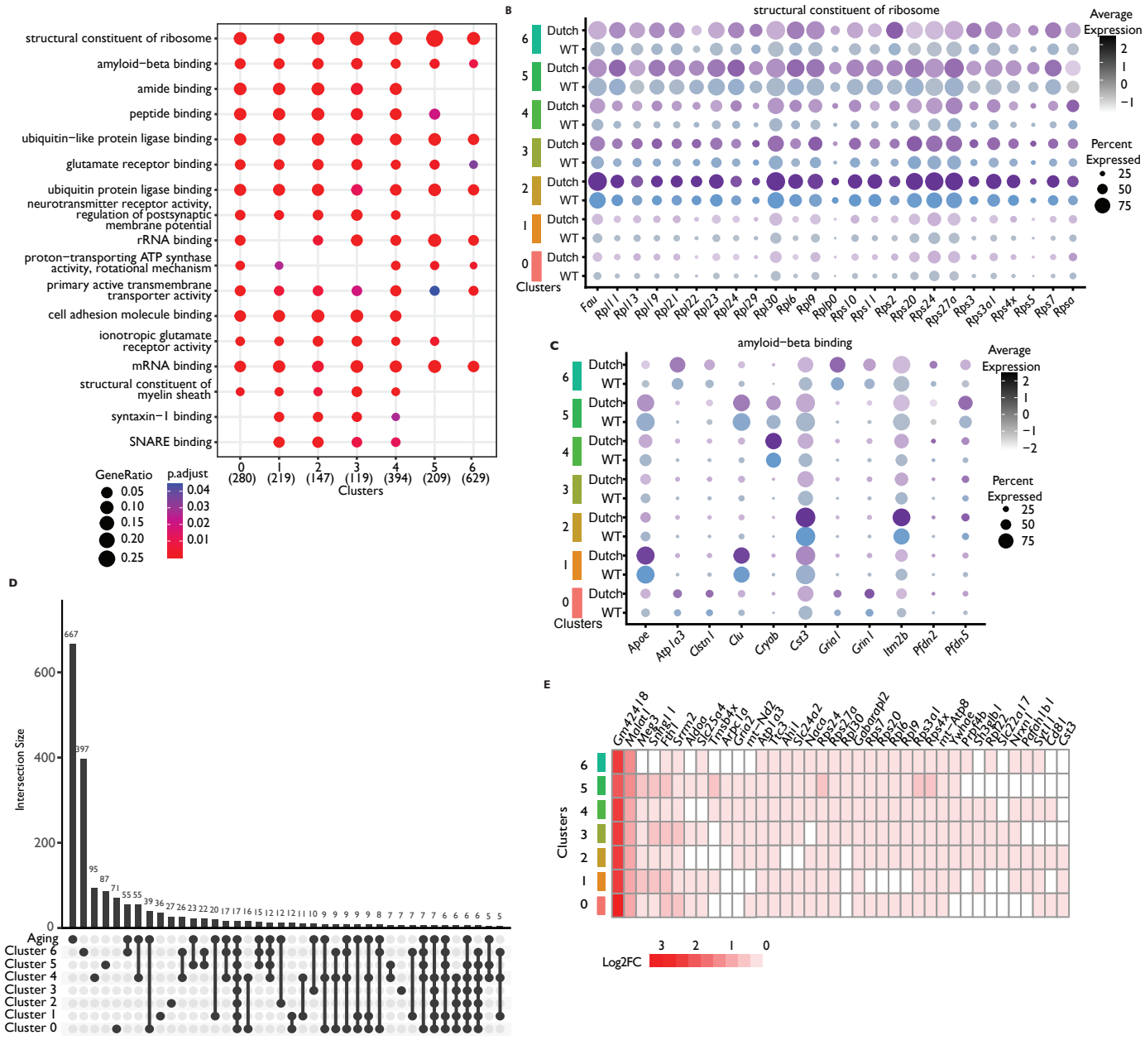
structural constituent of ribosome
amyloid−beta binding
amide binding
peptide binding
ubiquitin−like protein ligase binding
glutamate receptor binding
ubiquitin protein ligase binding
neurotransmitter receptor activity, regulation of postsynaptic membrane potential
rRNA binding
proton−transporting ATP synthase activity, rotational mechanism
primary active transmembrane transporter activity
cell adhesion molecule binding
ionotropic glutamate receptor activity
mRNA binding
structural constituent of myelin sheath
syntaxin−1 binding
SNARE binding
0 (280)
1 (219)
2 (147)
3 (119)
4 (394)
5 (209)
6 (629)
Clusters
GeneRatio
0.05
0.10
0.15
0.20
0.25
p.adjust
0.04
0.03
0.02
0.01
B
structural constituent of ribosome
Dutch
WT
Clusters
Average Expression
2
1
0
−1
Percent Expressed
25
50
75
Fau
Rpl11
Rpl13
Rpl19
Rpl21
Rpl22
Rpl23
Rpl24
Rpl29
Rpl30
Rpl6
Rpl9
Rplp0
Rps10
Rps11
Rps2
Rps20
Rps24
Rps27a
Rps3
Rps3a1
Rps4x
Rps5
Rps7
Rpsa
C
amyloid−beta binding
Average Expression
2
1
0
−1
−2
Percent Expressed
25
50
75
Apoe
Atp1a3
Clstn1
Clu
Cryab
Cst3
Grid1
Grin1
Itm2b
Pfdn2
Pfdn5
D
Intersection Size
667
397
95
87
71
55
55
39
36
27
26
23
22
20
17
17
16
15
12
12
12
11
10
9
9
9
9
9
8
7
7
7
7
7
6
6
6
6
5
5
Aging
Cluster 6
Cluster 5
Cluster 4
Cluster 3
Cluster 2
Cluster 1
Cluster 0
E
Gm42418
Malat1
Meg3
Snhg11
Ftl1
Srrm2
Aldoa
Scp2scp4
Tmsb4x
Atpc1a
Gria2
mt−Nd2
Atp1b3
Tcf3
Ahi1
Slc24a2
Nacc2
Rps24
Rps27a
Rpl30
Gabbr1
Rps27
Rpl26
Rpl9
Rpl3a1
Rps4x
mt−Atp8
Ywhae
Prnp
Sh3gl1
Sh3gl3
Rpl22
Rpl22a1
Nrxn1
Pdlim1
Stx1b
Cd81
Cst3
Clusters
Log2FC
3
2
1
0

Figure 6

Figure 6. Microglia transcriptomic profiles are similar between Dutch and wildtype mice. (A) UMAP plot showing sub-clustering analysis results for Cluster 2 microglia, identifying 3 subpopulations of microglia with UMAP plot split by genotype to the right. **(B)** UMAP plots showing expression of previously identified microglial signatures; DAM(*33*), homeostatic, IFN and MHC(*34*). **(C)** Violin plots showing expression across subclusters by genotypes of selected homeostatic microglial genes. (Wildtype, 1 male and 3 female; Dutch, 3 male and 1 female).

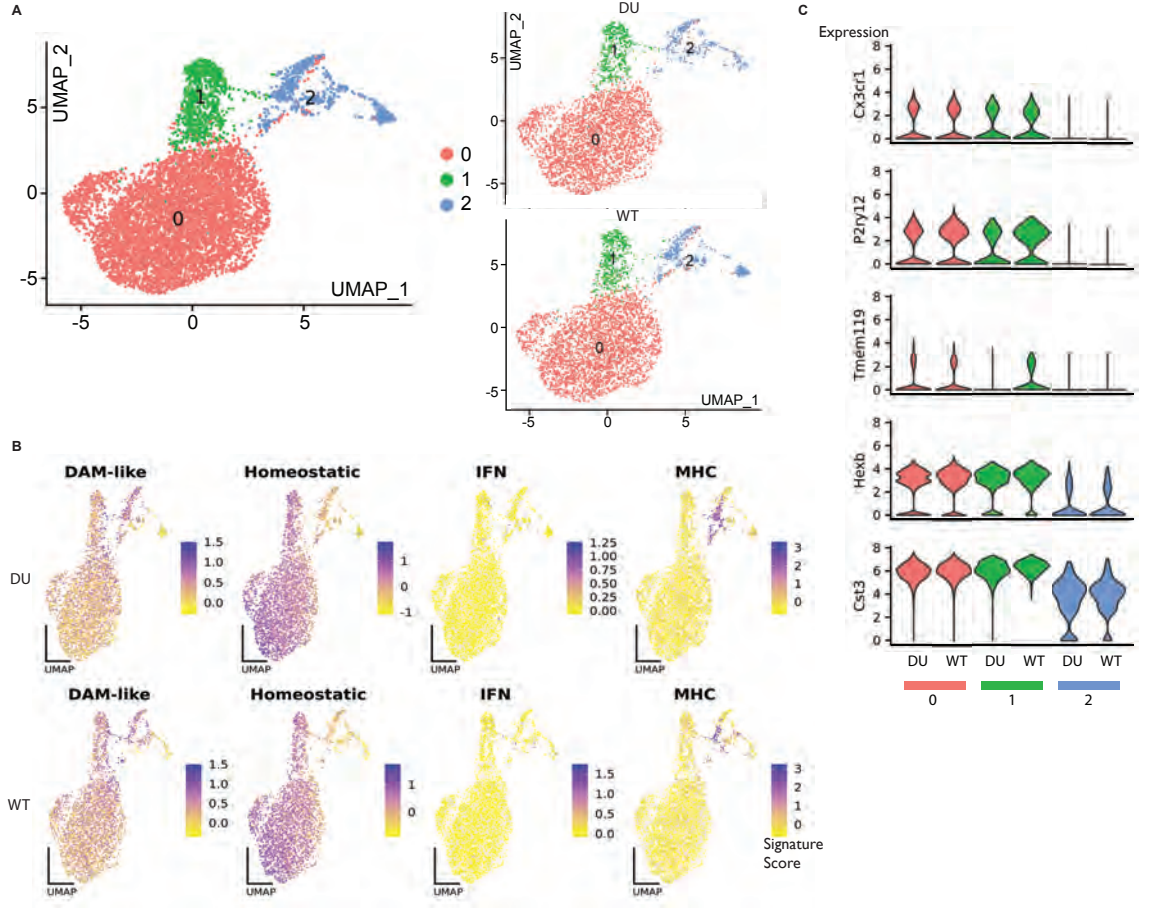
A
UMAP_2
UMAP_1
0
1
2
DU
WT
B
DAM-like
Homeostatic
IFN
MHC
DU
WT
UMAP
Signature Score
C
Expression
Cx3cr1
P2ry12
Tmem119
Hexb
Cst3
DU
WT

Figure 7

Figure 7. Transcriptional profile of Cluster 6 excitatory neurons is altered in Dutch mice. (A) Volcano plot of genes enriched in Cluster 6 as calculated by pseudobulk differential expression analysis. Red genes are Log2FC > 0.25 and adj. p-value < 0.05, blue Log2FC < 0.25 and adj. p-value < 0.05, green genes are Log2FC > 0.25 and adj. p-value > 0.05, and grey genes are Log2FC < 0.25 and adj. p-value > 0.05. **(B-C)** GO term analysis of **(B)** upregulated and **(C)** downregulated genes enriched in Cluster 6 (adj. p-value < 0.05) using metascape(*91*). **(D)** Dot plot of DEGs unique to Cluster 6. (Wildtype, 1 male and 3 female; Dutch, 3 male and 1 female).

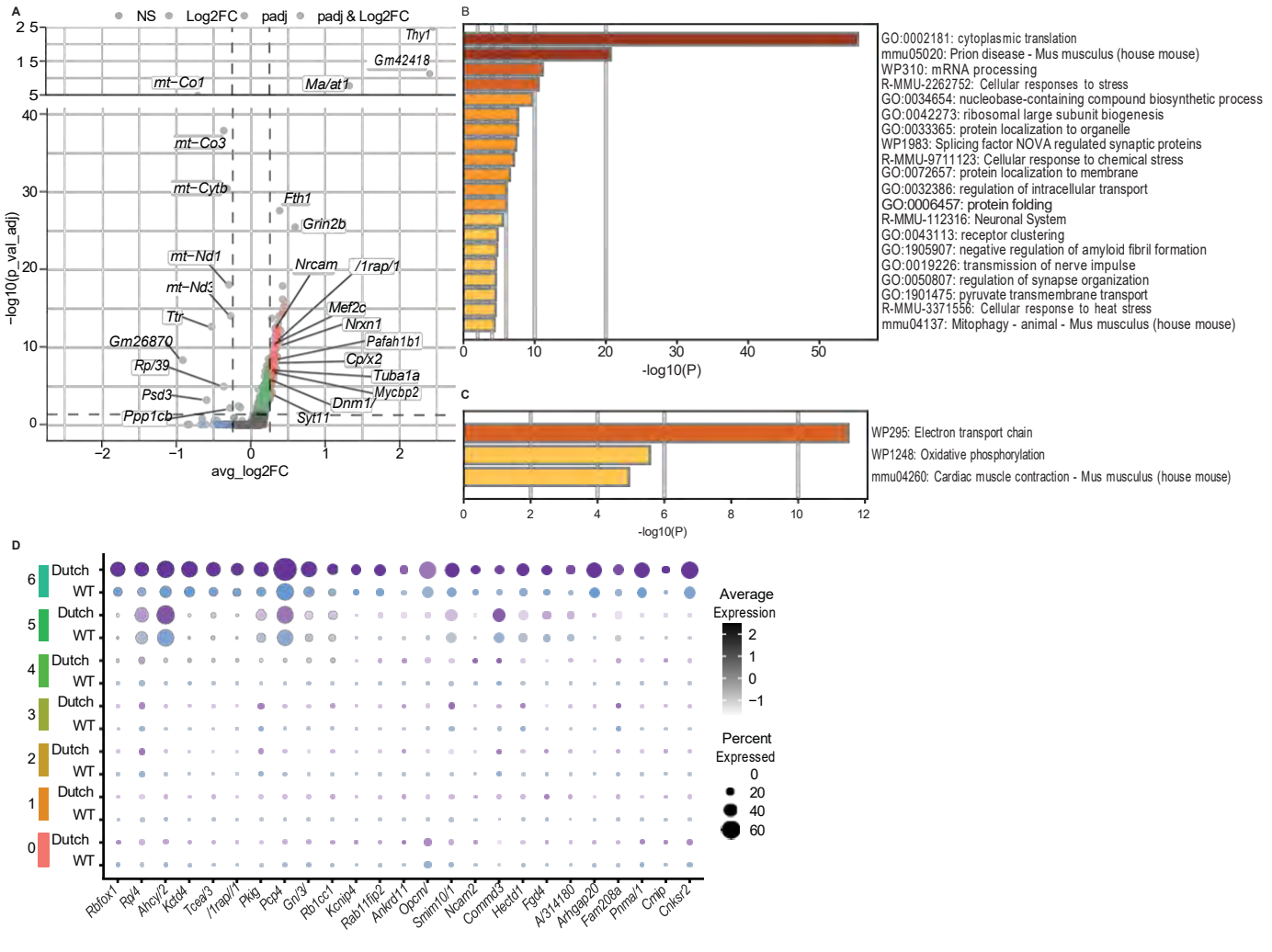
A
NS
Log2FC
padj
padj & Log2FC
Thy1
Gm42418
mt−Co1
Ma/at1
mt−Co3
mt−Cytb
Fth1
Grin2b
mt−Nd1
Nrcam
/1rap/1
mt−Nd3
Mef2c
Ttr
Nrxn1
Gm26870
Pafah1b1
Rp/39
Cpx2
Tuba1a
Psd3
Mycbp2
Dnm1/
Ppp1cb
Syt11
−log10(p_val_adj)
avg_log2FC
B
GO:0002181: cytoplasmic translation
mmu05020: Prion disease - Mus musculus (house mouse)
WP310: mRNA processing
R-MMU-2262752: Cellular responses to stress
GO:0034654: nucleobase-containing compound biosynthetic process
GO:0042273: ribosomal large subunit biogenesis
GO:0033365: protein localization to organelle
WP1983: Splicing factor NOVA regulated synaptic proteins
R-MMU-9711123: Cellular response to chemical stress
GO:0072657: protein localization to membrane
GO:0032386: regulation of intracellular transport
GO:0006457: protein folding
R-MMU-112316: Neuronal System
GO:0043113: receptor clustering
GO:1905907: negative regulation of amyloid fibril formation
GO:0019226: transmission of nerve impulse
GO:0050807: regulation of synapse organization
GO:1901475: pyruvate transmembrane transport
R-MMU-3371556: Cellular response to heat stress
mmu04137: Mitophagy - animal - Mus musculus (house mouse)
-log10(P)
C
WP295: Electron transport chain
WP1248: Oxidative phosphorylation
mmu04260: Cardiac muscle contraction - Mus musculus (house mouse)
-log10(P)
D
Dutch
WT
Average Expression
Percent Expressed
Rbfox1
Rpl4
Ahcyl2
Kctd4
Tcea3
/1rap/1
Pkig
Pcp4
Gng3
Rb1cc1
Kcnip4
Rab11fip2
Ankrd11
Opcml
Smim10/1
Ncam2
Commd3
Hectd1
Fgd4
A/314180
Arhgap20
Fam208a
Prrma/1
Crmp
Cnksr2

Figure 8

Figure 8. Fewer mitochondria were present in presynaptic boutons at excitatory synapses in the CA1 of 12-month-old Dutch mice compared to wildtype. **(A)** Electron micrographs showing representative examples of presynaptic mitochondria (blue masks). **(B)** Curved presynaptic mitochondria demonstrate a bend of at least 90°. Straight presynaptic mitochondria did not exhibit any curvature. Scale bar = 500 nm. **(C)** Total number, **(D)** number of straight mitochondria, **(E)** number of curved mitochondria, **(F)** percentage of curved mitochondria, **(G)** average diameter, and **(H)** number of layers traversed by each mitochondrion in wildtype and Dutch mice. Data are mean ± SD from n = 4 wildtype (2 male and 2 female) and n = 5 (4 male and 1 female) Dutch mice.

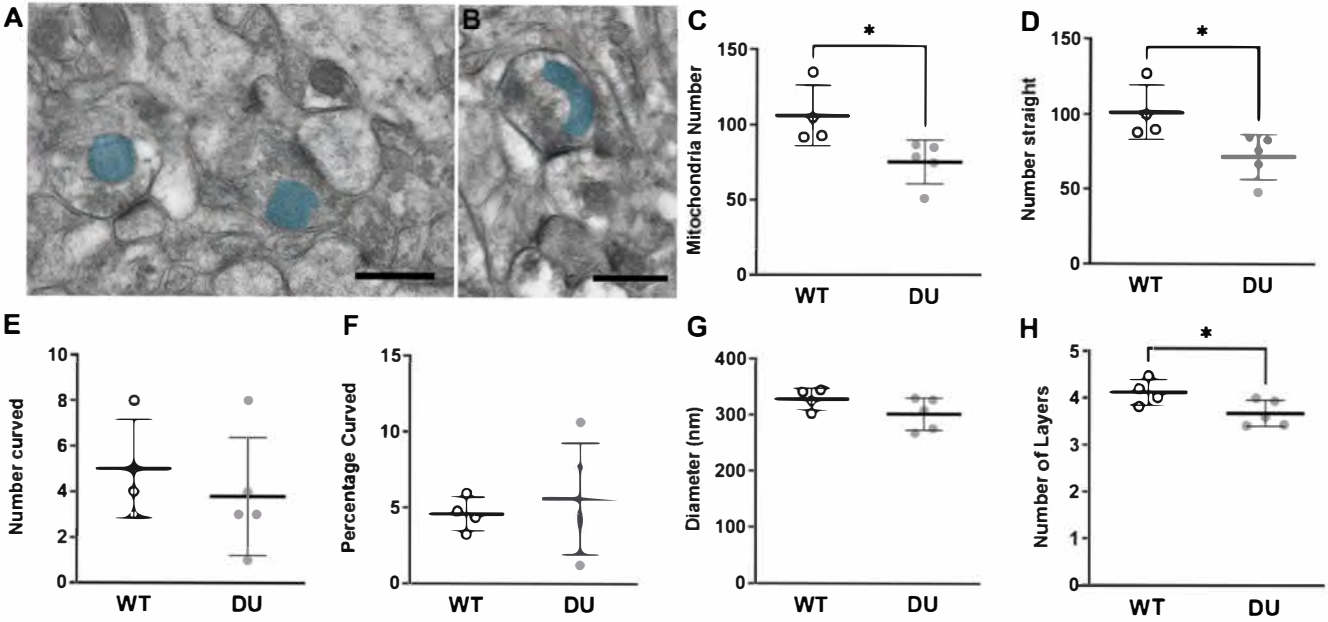
A
B
C
Mitochondria Number
150
100
50
0
*
WT
DU
D
Number straight
150
100
50
0
*
WT
DU
E
Number curved
10
8
6
4
2
0
WT
DU
F
Percentage Curved
15
10
5
0
WT
DU
G
Diameter (nm)
400
300
200
100
0
WT
DU
H
Number of Layers
5
4
3
2
1
0
*
WT
DU